Transition state vibrational level thresholds for the dissociation of triplet ketene

Sang Kyu Kim,[a] Edward R. Lovejoy,[b] and C. Bradley Moore
Department of Chemistry, University of California at Berkeley
and Chemical Sciences Division of the Lawrence Berkeley Laboratory, Berkeley, California 94720

Rate constants for the unimolecular dissociation of ketene (CH_2CO) and deuterated ketene (CD_2CO) have been measured at the threshold for the production of CH_2 ($\tilde{X}\ ^3B_1$) or CD_2 ($\tilde{X}\ ^3B_1$) and CO ($\tilde{X}\ ^1\Sigma^+$) by photofragmentation in a cold jet. The rate constant increases in a stepwise manner as energy increases. This is in accord with the long-standing premise that the rate of a unimolecular reaction is controlled by flux through quantized transition-state thresholds at each energy level for vibrational motion orthogonal to the reaction coordinate. The first step in rate constant and/or photofragment excitation (PHOFEX) spectrum gives accurate values for the barrier to dissociation above the zero-point energy of the products, 1281 ± 15 cm^{-1} for CH_2CO and 1071 ± 40 cm^{-1} for CD_2CO. The measured rate constants are fit by Rice–Ramsperger–Kassel–Marcus (RRKM) theory. The vibrational frequencies at the transition state obtained from the fits are compared with *ab initio* results. Vibrational motions at the transition state orthogonal to the reaction coordinate are also revealed in CO product rotational distributions. Calculations using an impulsive model which includes vibrational motions at the transition state reproduce the experimental dependence of the PHOFEX spectra on the CO J state quite well. The small dependence of rate constant on jet temperature (4–30 K) indicates that the K_a quantum number for rotation about its symmetry axis is conserved in the energized ketene molecule. © *1995 American Institute of Physics.*

I. INTRODUCTION

Transition-state theory (TST) was developed in the 1930's[1] and has been widely used in describing chemical reaction rates. TST is a statistical theory based on the fundamental assumptions that there is a local equilibrium between reactants and molecules crossing the transition state toward products along the reaction coordinate and that the molecule crossing through the transition state proceeds to products without recrossing. Even though TST has been enormously successful, the validity of these fundamental assumptions has been debated for decades. Rate constants may be calculated rigorously, given an exact potential energy surface (PES), by solving the Schrödinger's equation for the full quantum-state-resolved scattering matrix, calculating the cumulative reaction probability (CRP) as a function of total energy and angular momentum, and averaging over the distributions of initial energy and quantum state.[2,3] Miller has derived a rigorous quantum mechanical formulation which allows the CRP to be calculated directly from computations on a grid in the region of the transition state without explicitly calculating the scattering matrix, a "transition-state theory" without approximations.[4–7] Truhlar and co-workers[3] and Miller and co-workers[6] reported steplike structures in such rigorously calculated CRP's for the $H+H_2$ reaction; this shows that the CRP is controlled by quantized vibrational thresholds at the transition state as in the not so rigorous TST. Similar structures have also been calculated for $H+O_2$ by Leforestier and Miller[8] and in a more approximate way for $O+H_2$ (Ref. 9) and $H+H_2$ (Ref. 10) by Bowman. In experimental rate studies, since the initial conditions for bimolecular reactions are averaged over total angular momentum (impact parameter) and usually over thermal distributions of initial energy and quantum state, these structures are predicted to be completely smoothed out.[11] However, for unimolecular reactions, much of this averaging may be eliminated experimentally and the possibility exists to observe these quantized thresholds at the transition state.

The Rice–Ramsperger–Kassel–Marcus (RRKM) theory is a microcanonical ensemble version of transition state theory for treating unimolecular reaction rates.[12] RRKM theory is based on the additional assumptions that all vibrational states in the excited molecule are equally probable and that the vibrational energy flows freely among the different degrees of freedom at a rate much faster than the reaction rate. In RRKM theory, the rate constant for total energy E and total angular momentum J is given by

$$k(E,J) = \frac{W(E,J)}{h\rho(E,J)}, \tag{1}$$

where $W(E,J)$ is the number of energetically accessible states for vibration orthogonal to the reaction coordinate at the transition state, $\rho(E,J)$ is the density of vibrational states of the reactant, and h is Planck's constant. The rate constant increases stepwise as the energy increases through each vibrational level or threshold at the transition state. This step structure from $W(E,J)$ is apparently not an artifact of treating motion along the reaction coordinate classically since the

---

[a] Present address: Division of Chemistry and Chemical Engineering, California Institute of Technology, Pasadena, California 91125.
[b] Permanent address: NOAA/ERL/Aeronomy, R/E/AL-2, 325 Broadway, Boulder, Colorado 80303.

quantum treatments of CRP[2–10] exhibit quite similar structures. RRKM theory presumes that motion along the reaction coordinate is decoupled from the bound vibrational motions at the transition state. The passage through the transition state is then vibrationally adiabatic, and the vibrational levels are defined over a sufficiently broad region near the transition state to give well-defined reaction thresholds or quantized channels connecting reactant to products.

The RRKM theory has been used widely for many decades, and yet because of the lack of knowledge about potential energy surfaces (PES) in the vicinity of the transition state, vibrational frequencies at the transition state have been guessed or simply fit to explain thermally averaged experimental results. Due to the difficulty of resolving spectra of highly vibrationally excited reactant states, the density of reactant states in Eq. (1) has usually been estimated from data at much lower energies rather than measured directly. Recent spectroscopic studies have shown that the actual density of states for a number of small molecules [HCCH (Ref. 13), HFCO (Ref. 14), D_2CO (Ref. 15), CH_3O (Ref. 16), NO_2 (Refs. 17 and 18)] is three to ten times higher than predicted by estimates based on levels at significantly lower energy.

With the recent development of molecular beams and lasers, it is now possible to measure rate constants for reactants with well-defined initial conditions. A pulsed jet expansion is used to minimize the internal thermal energy and angular momentum of the molecule in its ground state, while high-resolution lasers are used to excite the molecule to well-defined reactant states and probe the fragments with quantum-state resolution. In addition, recent high-level quantum mechanical calculations now provide quantitative predictions for the properties of transition states of small molecules.[19] Therefore, unimolecular reaction rate theories are being subjected to more stringent tests. Using a variety of spectroscopic techniques such as overtone excitation, photon excitation followed by internal conversion, and stimulated emission pumping (SEP), kinetic studies of molecules prepared in well-defined quantum states have been carried out for several unimolecular reactions.[20–22]

RRKM theory, Eq. (1), predicts that the rate constant increases by steps with an amplitude equal to $1/[h\rho(E,J)]$ as the energy is increased through each vibrational level of the transition state. Recently, steplike structures in a rate constant have been reported for the unimolecular dissociation of ketene on its triplet surface.[23] Since there is a small barrier for this reaction, the transition state is well defined at the saddle point of the PES along the reaction coordinate, and the steps in rate constants have been attributed to vibrational level thresholds of the transition state. Structures in rate constants have also been reported for some barrierless unimolecular reactions. Zewail and co-workers have noted nonmonotonic features in rate constants for NCNO dissociation.[24] Wittig and co-workers reported steplike structures in rate constants for NO_2 dissociation and ascribed those steps to vibrational levels of a variational transition state which tightens as energy increases just 100 cm^{-1} above the reaction threshold.[18,25] For the same reaction, Tsuchiya and co-workers report that the rate constant increases stepwise when a new rotational product channel opens just 5
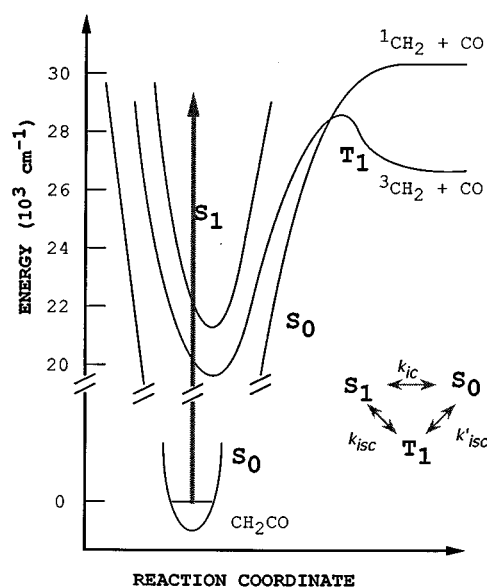

FIG. 1. The three lowest potential energy surfaces of ketene along the reaction coordinate. The ketene molecule is excited by a UV laser pulse to the first excited singlet state (S_1), undergoes internal conversion to S_0 and intersystem crossing to T_1, and dissociates into $^1CH_2$ ($\tilde{a}$ $^1A_1$)+CO (singlet channel) or $^3CH_2$ ($\tilde{X}$ $^3B_1$)+CO (triplet channel) fragments.

cm^{-1} above threshold.[17,26] Thus the transition state must move from loose to tight within a few tens of cm^{-1}.

The three lowest electronic states of ketene are the ground singlet state (S_0), the first excited singlet state (S_1), and the first triplet state (T_1). The ketene molecule in its ground state is UV laser excited ($S_1 \leftarrow S_0$), internally converts and/or intersystem crosses, and dissociates into methylene and CO products, Fig. 1.[22] The ketene molecule dissociates into singlet methylene and CO fragments (singlet channel) on the barrierless ground singlet potential energy surface with a threshold energy of 30 116 cm^{-1},[27–29] while it dissociates into triplet methylene ($^3CH_2$) and CO fragments on the triplet surface which has a small barrier about 1300 cm^{-1} above the triplet products and 2000 cm^{-1} below the singlet products.[30,31] Recently, unimolecular reaction of ketene on singlet and/or triplet channels has been studied extensively and provided a good example for testing a variety of statistical theories.[22,27–34]

In this work, the rate constants for dissociation of rotationally cold (4 K) ketene to $^3CH_2$+CO are measured as a continuous function of energy. The quantized transition state vibrational thresholds are revealed in clear steplike structures observed in the unimolecular dissociation rate constants. This is consistent with the fundamental postulates of transition state (RRKM) theory and provides a quantitative test of unimolecular reaction rate theory.

II. EXPERIMENT

Ketene (CH_2CO) was prepared by passing acetic anhydride through a red-hot quartz tube, trapped at 77 K, and distilled from 179 to 77 K twice before use. Deuterated ketene (CD_2CO) was prepared by the same method from

deuterated acetic anhydride (Sigma, >99.0% assay). Ketene was stored at 77 K. During experiments, the ketene vapor pressure was kept at 50 Torr by a hexanes slush bath (179 K). Helium carrier gas was bubbled through the sample and the gas mixture was expanded through the 0.5 mm diameter orifice of a pulsed nozzle into the vacuum chamber. The backing pressure of the carrier gas was 1.5 atm and the background pressure in the vacuum chamber was maintained at 10^{-4} Torr when the nozzle was on. Ketene was rotationally cooled by the supersonic expansion and the rotational temperature of ketene in the experiment was estimated to be about 4 K.[27] In some experiments the backing pressure of the carrier gas was varied from 260 Torr to 2.2 atm to vary the rotational temperature of ketene in the supersonic jet. A mixture of 100 ppm of CO in He was expanded and fluorescence excitation spectroscopy used to estimate the temperature of the molecular beam.

The photolysis laser was a frequency-doubled dye laser (Lambda Physik FL2002E; 0.2 cm^{-1} linewidth) pumped by the second harmonic output of a Q-switched Nd:YAG laser (Spectra-Physics DCR-4). DCM, LDS698, and mixtures of those dyes in methanol were used in the dye laser to generate 30–50 mJ/pulse of energy in the 680–720 nm range. The UV energy was 6–10 mJ/pulse in the 340–360 nm region, with a 0.4 cm^{-1} linewidth and a 7 ns duration. The frequency of the dye laser output was calibrated with an accuracy of ±0.5 cm^{-1} using the optogalvanic spectrum of Ne gas. During scans the direction and intensity of the UV laser output were actively maintained and maximized, respectively, by an Inrad Autotracker II with a KDP crystal. The UV laser output was almost completely separated from the fundamental visible laser pulse (99.9% attenuated) through three reflections from UV dichroic mirrors before it entered the vacuum chamber.

Tunable vacuum UV (VUV) was generated for the laser-induced fluorescence (LIF) probing of CO fragment in the ($\tilde{A}$ $^1\Pi$–$\tilde{X}$ $^1\Sigma^+$) ($v'=3-v''=0$) band. The output of a dye laser (Lambda Physik FL3002E; linewidth ≈0.2 cm^{-1}, pulse length ≈7 ns; 15–20 mJ/pulse in the 430–450 nm range with coumarin-440 dye in methanol) pumped by the third harmonic output of another Q-switched Nd:YAG laser (Continuum YG682-10) was frequency tripled in Xe gas to generate VUV in the 143–150 nm range. The efficiency of tripling is about 10^{-6}.[35] The fundamental dye laser output was focused by a fused silica lens (f.l.=7 cm) into the center of a 10 cm long tripling cell filled with 20–40 Torr of Xe gas. The VUV was collimated by a CaF$_2$ lens (f.l.=8 cm) located at the exit of the tripling cell.

The photolysis and probe lasers propagated colinearly from opposite ends of the vacuum chamber and crossed the molecular beam pulse at 90°. The interaction region, defined by the overlap of the lasers, was centered 3–4 cm from the nozzle orifice. The polarizations of both laser pulses were parallel to the jet axis and perpendicular to the fluorescence detection axis (vide infra). A small portion of the photolysis laser intensity was reflected from the entrance window of the vacuum chamber, detected by a fast-response photodiode, and used to normalize for photolysis laser intensity fluctuations. The VUV probe laser passed through the molecular beam, was partially reflected from the exit window inside the

vacuum chamber, scattered from a LiF diffuser, struck a solar blind VUV PMT (EMR 542G-08-19, LiF window), and produced a signal to normalize for VUV intensity fluctuations. The linearity of normalization was carefully checked.[32]

The nozzle valve driver (Newport BV100) and two Nd:YAG lasers were triggered by an SRS DG535 pulse generator at a 10 Hz repetition rate. Scattered photolysis laser light detected by a fast photodiode was used to trigger a boxcar (SR250 from SRS). The gate output of the boxcar was delayed by the desired amount with respect to the trigger signal, amplified, and used to trigger the Q switch of the other Nd:YAG laser. The molecular beam pulse was synchronized with the laser pulses by the internal delay function of the nozzle valve driver.

LIF of the CO product was detected by a solar-blind VUV photomultiplier tube (PMT) (EMR 542G-09-19, 50 mm diam MgF$_2$ window) 5 cm away from the interaction region (vide supra). A cultured quartz window in front of the VUV PMT absorbed scattered VUV laser light. PMT signals were preamplified by 50 times (Hewlett-Packard, 8447D OPT 001), sampled and integrated by a boxcar (SR250), digitized by an A/D converter (DASH-8 Metrabyte), and stored in a microcomputer (IBM PC/XT).[36] Both photolysis and probe laser frequencies were controlled by the same computer.

Rate constants for photodissociation of ketene were determined by measuring the appearance rates of CO fragments. The VUV probe laser frequency was fixed at a specific rovibronic transition of the CO product and the CO LIF signal was monitored while scanning the delay time between pump and probe lasers at a fixed pump laser frequency. The delay time was scanned using SR265 software to control the delay between trigger signal and gate output of the boxcar via an SR245 computer interface. Data acquisition was controlled by the same software.

CO product rise curves were obtained at photolysis energies for which rate constants were in the 10^6–5×10^7 s^{-1} range. Proper alignment of photolysis and probe lasers is critical for accurate rate measurements. The alignment was validated by recording the CO product rise curve at a photolysis energy for which the CO rise is <50 ns. For a 20 mm^2 UV laser beam cross section, the signal remained at its maximum until 1.0 μs when the UV-excited sample began to move beyond the probing zone defined by the cross section of the VUV probe laser beam (7–12 mm^2). For the measurement of rates <5×10^6 s^{-1}, the cross section of the pump laser beam was expanded by about four times to give uniform detection out to 2.0 μs, Fig. 2. Because of the decrease in the photolysis laser energy density, the signal-to-noise (S/N) ratio decreased and yielded larger uncertainties. Rate constants as small as 1.0×10^6 s^{-1} were measured without any correction to the raw experimental data.

Each CO product rise curve was averaged over 15–20 scans and measured three times at each photolysis energy. Rate constant measurements were carried out as a function of photolysis energy at 2–4 cm^{-1} intervals. To check the reproducibility of the data, the three different measurements at each photolysis energy were carried out on different days with a new alignment of laser beams.
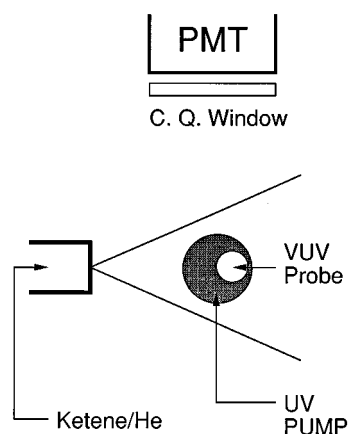
FIG. 2. Cross section of the VUV LIF detection geometry in the molecular beam chamber. A cultured quartz window (C.Q.) is used in front of the VUV PMT to reduce the scattered probe laser light. For measurements of rate constants less than 5×10^6 s^{-1}, the expanded photolysis laser is overlapped with the VUV probe laser in the downstream portion of the molecular jet. The distances of the PMT and the orifice of the nozzle from the interaction region are about 5 and 3 cm, respectively. The diameters of UV pump and VUV probe lasers are about 10 and 4 mm, respectively.
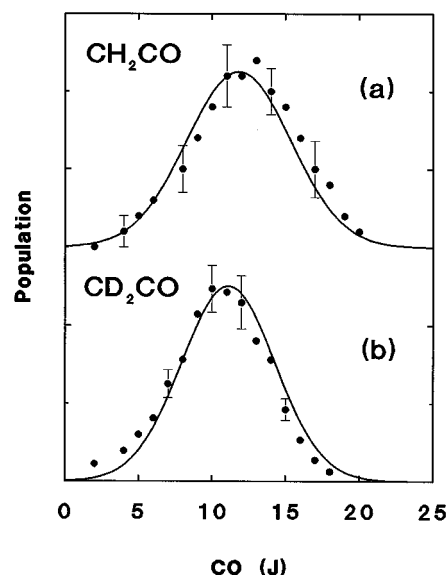

FIG. 3. CO product rotational distributions from the dissociation of ketene. The solid lines are calculated from *ab initio* data as in Ref. 30: (a) CH$_2$CO at 28 250 cm^{-1}, 1 μs; (b) CD$_2$CO at 28 410 cm^{-1}, 1 μs.

Photofragment excitation (PHOFEX) spectra were obtained by monitoring the LIF signal for a single CO(v,J) state while the photolysis laser frequency was scanned. The delay time between the photolysis and probe lasers was fixed with a time jitter of less than 5 ns. PHOFEX curves were obtained with 0.5–1 cm^{-1} steps of the photolysis laser frequency. Each data point was averaged for 10–20 laser shots and PHOFEX curves were averaged for 3–5 scans.

III. RESULTS

A. CO product rotational distributions

CO product rotational distributions, obtained from rovibrationally resolved VUV LIF spectra for CO product by the same method as described in Ref. 30, are shown for CH$_2$CO and CD$_2$CO at photolysis energies of 28 250 cm^{-1} and 28 410 cm^{-1} in Fig. 3. The rotational distributions are approximately Gaussian-shaped and peak near $J=12$ for CH$_2$CO and $J=11$ for CD$_2$CO. The CO fragment acquires angular momentum from the forces exerted as it passes through the exit valley of the potential energy surface. An impulsive force along the C–C bond at the geometry of the transition state combined with the vibrational momenta at the transition state model the observed distributions quite well.[30]

B. Rate constants, *k*(*E*)

CO product rise curves are shown in Figs. 4 and 5. As previously,[31] the rate constants measured for different J states of CO such as 13 and 6 are the same as those for $J=12$ within experimental error. Since the $Q(12)$ transition is one of the well isolated peaks in the LIF spectrum and probes the most populated level of CO, it has been used for all rate constant measurements.

When the CO fragment is probed at a long delay time after UV excitation, collisional rotation-to-translation energy transfer may occur. Figure 4 compares the CO rise curves for $J=6$ and 12. Relaxation from high to low J is clearly observed beginning at 2.5 μs delay, significantly after the volume of excited gas begins to move beyond the probe laser beam.

The CO product rise curves are least-squares fit by a single exponential. The pulse widths of pump and probe lasers (7 ns) are convoluted in the fitting for rates faster than 5×10^7 s^{-1} as in Ref. 31. The standard deviation for the least-
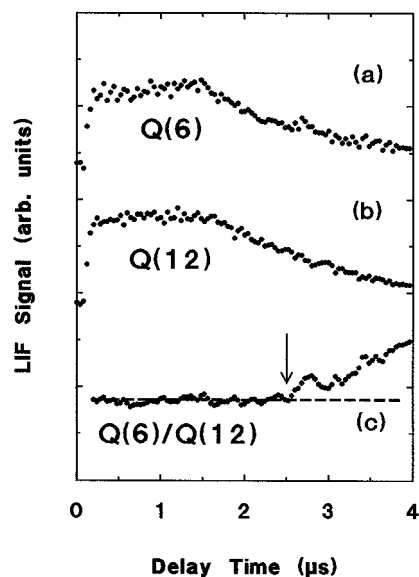

FIG. 4. CO ($v=0$) product rise curves for CD$_2$CO dissociation at 28 900 cm^{-1} ($k \approx 3 \times 10^7$ s^{-1}). (a) $J=6$; (b) $J=12$; (c) ratio of the CO $J=6$ and $J=12$ signals. The LIF intensity for $J=6$ is about 5 times less than that for $J=12$. The delay time at which rotational relaxation starts is marked by an arrow on (c). The UV beam cross section was ~80 mm^2.
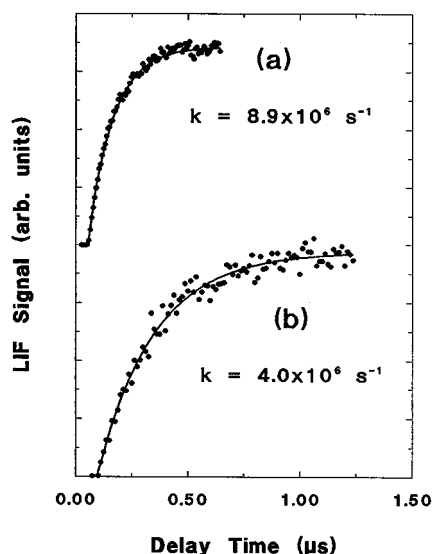
FIG. 5. $J = 12$ CO product rise curves with single exponential fits. (a) CH$_2$CO at 28 423 cm^{-1}, and (b) CD$_2$CO at 28 500 cm^{-1}.

FIG. 7. Rate constant for CD$_2$CO dissociation as a function of the photolysis energy. The CO($v = 0$, $J = 12$) PHOFEX curve ($\Delta t = 1.7$ μs) is shown in the reaction threshold region; its intensity is arbitrarily scaled. The solid line is a RRKM fit using the parameters in Table V.

squares fit to an individual CO rise curve is much less than the deviations between measurements made on each of three different days and their mean. For CD$_2$CO, the rate constants within 40 cm^{-1} of threshold are too small to measure accurately.

Rate constants as a function of the photolysis energy, $k(E)$, are plotted as open circles in Figs. 6 and 7 for CH$_2$CO and CD$_2$CO, respectively. Error bars shown on selected data points are two times the estimated standard deviation of the mean of the three measurements from the true value. Distinct steps in $k(E)$ associated with the first few transition state
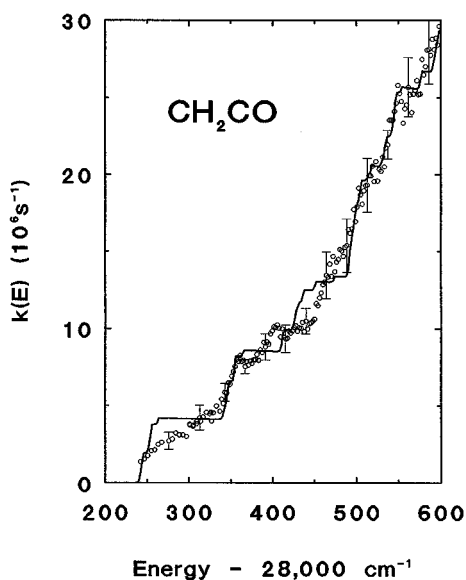
vibrational level thresholds are observed in the first 200–300 cm^{-1} region above the reaction thresholds for each isotope.

C. Photofragment excitation spectra

PHOFEX spectra probing the $Q(12)$ transition of CO from CH$_2$CO at 50 ns and from CD$_2$CO at 200 ns delay times are shown by curve (a) in Figs. 8 and 9. The PHOFEX signal can be expressed as

FIG. 6. Rate constant for CH$_2$CO dissociation as a function of the photolysis energy. The error bars on selected data points represent twice the standard deviation from three independent rate constant measurements. The solid line is a RRKM fit using parameters in Table V, but without tunneling.
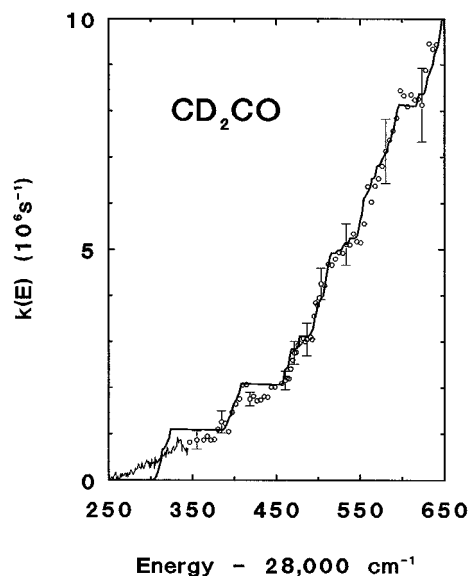

FIG. 8. PHOFEX curves. (a) CO($J = 12$), $\Delta t = 50$ ns; (b) $\{1 - \exp[-k(E) \times \Delta t]\}$ scaled for comparison to (a); (c) CO($J = 2$), $\Delta t = 50$ ns. The actual ratio of the yields of CO($v = 0$, $J = 12$) to CO($v = 0$, $J = 2$) is about 20:1 at 28 500 cm^{-1}.
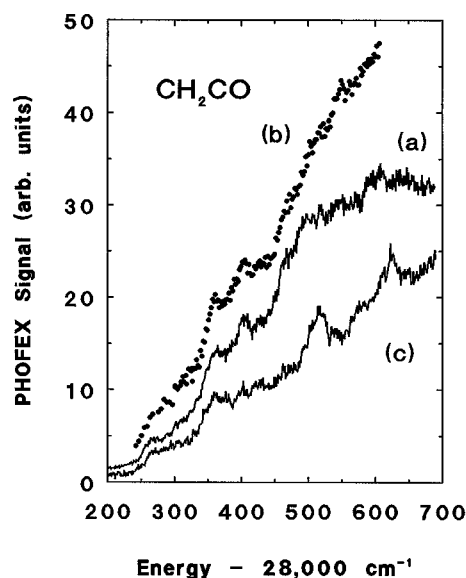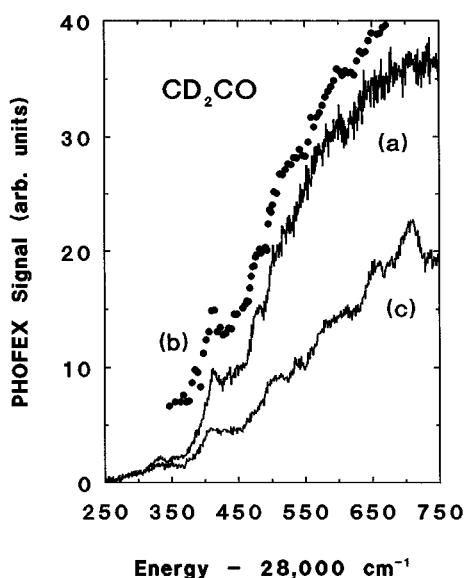
FIG. 9. PHOFEX curves. (a) CO($J=12$), $\Delta t=200$ ns; (b) $\{1-\exp[-k(E) \times \Delta t]\}$ scaled for comparison to (a); (c) CO($J=2$), $\Delta t=150$ ns. The actual ratio of the yields of CO($v=0$, $J=12$) to CO($v=0$, $J=2$) is about 20:1 at 28 500 cm^{-1}.

FIG. 10. The CO($v=0$, $J=12$) PHOFEX curves taken at 50 ns delay time at (a) solid line: at 2.2 atm ($T_{rot}=4$ K) and (b) squares: at 260 Torr ($T_{rot}=30$ K) backing pressure of carrier gas.

$$S(E,v,J_{CO}) \propto \sigma(E) P(E,v,J_{CO})\{1-\exp[-k(E) \times \Delta t]\}, \quad (2)$$

where S is the LIF intensity when probing the CO(v,J) product, $\sigma(E)$ is the absorption cross section of the parent molecule for photon energy E, $P(E,v,J_{CO})$ is the probability for the CO fragment to be formed in the (v,J_{CO}) quantum state, $k(E)$ is the ketene decay rate constant averaged over the ensemble of initial excited states of ketene, and Δt is the time delay between the pump and probe lasers.

The absorption spectrum of CH$_2$CO at room temperature is a diffuse structureless band for the $S_1 \leftarrow S_0$ transition.[37] Presumably, this is the result of fast internal conversion and intersystem crossing. The analysis of singlet CH$_2$ PHOFEX spectra shows that $\sigma(E)$ in the pulsed jet is nearly constant over ranges of several hundred cm^{-1} in photolysis energy.[27,34] Curves b in Figs. 8 and 9 show $\{1-\exp[-k(E) \times \Delta t]\}$ using directly measured $k(E)$ and the Δt of the PHOFEX spectrum. If $\sigma(E)$ and $P(E,v,J_{CO})$ are constant, then curves (a) and (b) should have the same shape. In the first 200–300 cm^{-1} above the reaction threshold, the positions and amplitudes of steps in curves (a) and (b) are the same. This confirms the structures observed in $k(E)$ and shows that $\sigma(E) \times P(E,v,J_{CO})$ is nearly constant over this small range of energy just above threshold. At higher photolysis energy, over 28 500 cm^{-1} for CH$_2$CO, $\{1-\exp[k(E) \times \Delta t]\}$ is still increasing with increasing energy while the experimental curve starts to level off. This deviation indicates a decrease in $\sigma(E) \times P(E,v,J_{CO})$. A more striking difference in shape is exhibited by PHOFEX curve (c) in Fig. 8 for CO($v=0$, $J=2$) which has a sharp peak near 28 500 cm^{-1} where the CO($v=0$, $J=12$) PHOFEX curve starts to level off. This peak and leveling off are consistent with a significant broadening of the product rotational distribution at this energy. The width of the CO rotational distribution is
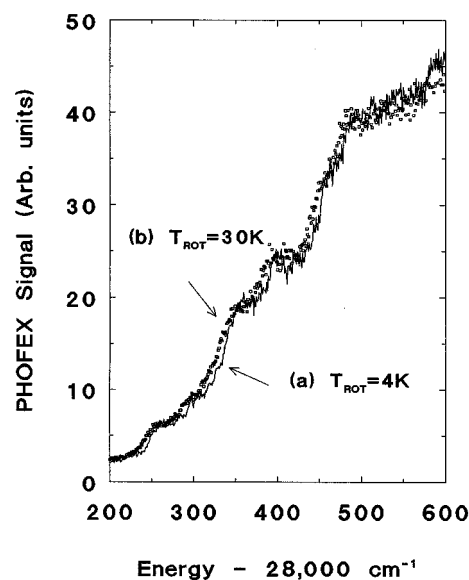
determined by the vibrational motion at the transition state.[30] Therefore, the comparison of PHOFEX curves for CO product with different J_{CO}'s gives a dynamically biased way to observe thresholds for transition-state vibrations which strongly influence CO rotation. The PHOFEX spectrum for CO($v=0$, $J=2$) from CD$_2$CO, Fig. 9, shows steps and peaks at higher photolysis energies where the structures in both $k(E)$ and the CO($v=0$, $J=12$) PHOFEX curve become washed out, thus revealing additional vibrational thresholds at the transition state.

CO($v=0$, $J=12$) PHOFEX curves taken at 4.0 ± 0.5 K and 30 ± 3 K (2.2 atm and 260 Torr backing pressure, respectively) are almost identical, Fig. 10. Although the actual rotational temperature of ketene in the molecular beam may be different from that of the CO used for calibration, it is clear that there is no dramatic effect of ketene rotational temperature on the rate constant in this range.

IV. ANALYSIS AND DISCUSSION

The observation of structures in $k(E)$ is consistent with the fundamental ideas of transition-state theory and RRKM theory. The application of the RRKM model to ketene is developed in the following sequence: (A) Coupling among the three lowest electronic states (S_1, S_0, T_1) for $E > 28\,000$ cm^{-1}; (B) Symmetry selection rules for the UV excitation and nonradiative transitions; (C) *Ab initio* transition-state geometry and vibrational frequencies;[38] (D) RRKM equations; and (E) RRKM fits.

A. Coupling of electronic states

Three electronic states of ketene are involved in the reaction dynamics, S_1, T_1, and S_0, Fig. 1. The *ab initio* calculations of Allen and Schaefer[38] give the zero-point levels of S_1 and T_1 at 21 195 and 19 150 cm^{-1} above that for S_0

with an estimated uncertainty of 700 cm^{-1}. The two excited electronic states have nearly identical equilibrium geometries[38] with the CCO frame bent in plane at an angle of 129 deg. The ground state is very different with a linear CCO frame that has considerably shorter bond lengths. At the 28 250 cm^{-1} energy of the barrier to formation of triplet products, the densities of vibrational states calculated using the Whitten–Rabinovitch approximation are $\rho(S_1) \approx 4$, $\rho(T_1) \approx 26$, and $\rho(S_0) \approx 1.4 \times 10^4$/cm^{-1}.[31] The sum of the densities of states, ρ_{total}, is thus dominated by $\rho(S_0)$.

There are no direct measurements of rate constants or matrix elements for couplings among these three electronic states. However it is most likely that with respect to nanosecond time scale phenomena all three are strongly coupled together.[27] For this to be so, it suffices for two of the three couplings among the three states to be strong. The $S_1 \leftarrow S_0$ spectrum[39] shows some possible vibrational structure with linewidths of about 200 cm^{-1} suggesting an upper limit of 4×10^{13} s^{-1} for the S_1 decay rate. There is no rotational fine structure or Q-branch feature observable; the latter would surely be seen unless the linewidth were at least 5 cm^{-1}. Thus S_1 must decay with a rate of at least 10^{12} s^{-1}. Therefore, the sum of the rates for internal conversion to S_0 and intersystem crossing to T_1 must lie in the range $4 \times 10^{13} > k_{\text{ic}} + k_{\text{isc}} > 10^{12}$ s^{-1}. At least one coupling, rate of transfer between electronic states, is large. Could the other two both be small?

If only k_{isc} were larger than 10^{12} s^{-1}, then the triplet could be populated directly from S_1 and decay without involving S_0 at a rate of at least $1/h\rho(T_1) = 10^9$ s^{-1} at threshold. Since the observed dissociation rate of the triplet at threshold is less than 4×10^6 s^{-1}, T_1 and S_0 must be coupled directly by k'_{isc} or indirectly by k_{ic} at greater than 10^9 s^{-1} so that the rate of dissociation on the triplet surface at threshold is controlled by the total density of vibronic levels, $1/h\rho_{\text{total}}$. Thus if only k_{isc} is larger than 10^{12} s^{-1}, one or both of k_{ic} and k'_{isc} must also be larger than 10^9 s^{-1}.

If only k_{ic} were larger than 10^{12} s^{-1}, then T_1 would equilibrate with the two singlets at a rate given approximately by $[\rho(S_1)/g_t\rho(T_1)]k_{\text{isc}} + k'_{\text{isc}}$ where g_t is the number of triplet spin states strongly coupled. If the rate of dissociation of a pure triplet state is faster than this equilibration rate, then the rate of dissociation of ketene would be limited by the intersystem crossing rate. The kinetic scheme, Fig. 1, gives a rate constant of $k_t = [(g_t\rho(T_1)/\rho(S_0)]k'_{\text{isc}} + [(\rho(S_1)/\rho(S_0)]k_{\text{isc}}$ for this case. The observed dissociation rate, Fig. 6, increases strongly with energy from 4×10^6 s^{-1} near the threshold for triplet dissociation, to 2×10^7 s^{-1} just 250 cm^{-1} higher in energy, to 3×10^8 s^{-1} 1866 cm^{-1} higher[29] at the singlet threshold. Since S_1 and T_1 have similar geometries and origins, the Franck–Condon factors for k_{isc} and therefore k_{isc} itself cannot depend strongly on energy. The second term in the expression for k_t cannot be responsible for the data in Fig. 6. Since T_1 and S_0 have very different geometries, a strong dependence of k'_{isc} on energy is likely. However, at the high levels of vibrational excitation in these two states, it is very unlikely indeed that the regular stepped increases in rate in Fig. 6 result from vibronic structure in k'_{isc}.

It appears far more likely that intersystem crossing is faster than dissociation, especially in the threshold region. In this case the wave functions for individual molecular eigenstates are a statistical mixture of S_1, T_1, and S_0 basis states given by

$$|\Psi_n\rangle = \sum_i \alpha_{ni}|S_{1i}\rangle + \sum_j \beta_{nj}|S_{0j}\rangle + \sum_k \gamma_{nk}|T_{1k}\rangle, \quad (3)$$

where the coefficients α_{ni}, β_{nj}, and γ_{nk} of the individual basis functions of each electronic state are related to the vibronic level densities by

$$\sum_i |\alpha_{ni}|^2 \approx \frac{\rho(S_1)}{\rho_{\text{total}}},$$

$$\sum_j |\beta_{nj}|^2 \approx \frac{\rho(S_0)}{\rho_{\text{total}}}, \quad \sum_k |\gamma_{nk}|^2 \approx \frac{g_t\rho(T_1)}{\rho_{\text{total}}}. \quad (4)$$

The eigenstates with the most S_1 character are preferentially excited by the UV laser pulse, since only S_1 states carry significant oscillator strength. The photolysis pulses (0.4 cm^{-1} linewidth; 7 ns duration) excite a set of about 6000 eigenstates with phase coherence among the S_1 coefficients extending only over about ten adjacent states. Thus statistical fluctuations[40] of the rate constants from eigenstate to eigenstate should be completely averaged out. The dissociation rate of ketene on the triplet surface is then given by the usual transition state theory expression, Eq. (1), with $\rho(E, J) = \rho_{\text{total}}$.

B. Symmetry selection rules

1. Conserved quantities

In the absence of external fields, total energy E_{tot} and total angular momentum (F, M_F) are conserved throughout the dissociation. Since the weak interaction is quite negligible on the microsecond time scale, parity with respect to inversion (Π) is also conserved. On the time scale of photodissociation, the nuclear spin (I, M_I) and nuclear spin symmetry (Γ_{ns}) are known to be conserved.[27] Therefore, the RRKM rate constant in Eq. (1) is more rigorously written as

$$k(E_{\text{tot}}, J, I, \Pi, \Gamma_{\text{ns}}) = \frac{W(E_{\text{tot}}, J, I, \Pi, \Gamma_{\text{ns}})}{h\rho(E_{\text{tot}}, J, I, \Pi, \Gamma_{\text{ns}})}, \quad (5)$$

where $\mathbf{F} = \mathbf{I} + \mathbf{J}$, $E_{\text{tot}} = E + E_{\text{thermal}}$ (the sum of the UV photon and thermal excitation in the jet), Π and Γ_{ns} are for the ketene molecule following UV excitation.

2. Angular momentum selection rules

The photodissociation of ketene on the triplet surface involves UV optical excitation ($S_1 \leftarrow S_0$), internal conversion ($S_0 \leftrightarrow S_1$), and intersystem crossing ($T_1 \leftrightarrow S_0, S_1$) as well as dissociation. The symmetry species for ketene in any electronic state are classified in the C_{2v} molecular symmetry (MS) group which is isomorphic with the G_4 CNPI group. This is a sensible approach even for the strongly bent transition-state geometry since its torsional barrier is so low[38] that operationally the overall symmetry of the total Hamiltonian is C_{2v}. Ketene is a slightly asymmetric prolate top. The magnitude of the projection of rotational angular

momentum $\mathbf{N}$ on the "a" axis, $|K|$, can be a nearly good quantum number and thus selection or propensity rules for K are given. The selection rules for angular momentum quantum numbers and wave function symmetries for each process follow.

(i) UV excitation ($S_1 \leftarrow S_0$)

The optical transition from $S_0(^1A_1)$ to $S_1(^1A_2)$ is electronically forbidden but vibronically allowed for electric dipole radiation. From A_1 vibronic symmetry in the S_0 ground state, A-type, parallel transition gives rise to a_2 vibrational states in S_1. B-type and C-type perpendicular transitions excite b_1 and b_2 vibrational states, respectively. The selection rules for total angular momentum and parity are

$$\Delta F = 0(F \neq 0), \pm 1; \quad + \leftrightarrow -.$$

With nuclear spin conserved, the selection rules become

$$\Delta J = 0(J \neq 0), \pm 1; \quad \Delta I = 0; \quad + \leftrightarrow -. \tag{6}$$

The selection rules for the K quantum number in the symmetric top limit are

$$\Delta K = K' - K'' = 0 \quad (A\text{-type, parallel});$$
$$\Delta K = K' - K'' = \pm 1 \quad (B\text{-, } C\text{-types, perpendicular}). \tag{7}$$

(ii) Nonradiative transitions

The symmetry of the wave function and the conserved quantities in Sec. IV B 1 are unchanged in nonradiative transitions. Thus internal conversion from A_1, B_2, and B_1 vibronic symmetries in S_1 gives rise to a_1, b_2, and b_1 vibrational states in S_0 with the selection rules

$$\Delta S = 0; \quad \Delta J = 0; \quad \Delta I = 0;$$
$$\Delta K = K - K' = 0; \quad + \leftrightarrow +, - \leftrightarrow -. \tag{8}$$

In the highly vibrationally excited S_0 states of ketene resulting from internal conversion, strong anharmonic and Coriolis couplings are expected. In the case of strong vibration–rotation coupling, K is not a good or nearly good quantum number. In the extreme case, K may be completely mixed thus giving molecular states with equal contributions from basis states with K from $-J$ to J. This is the limit usually assumed in applications of RRKM theory. The extent of K mixing has not previously been established experimentally for ketene; it will be seen below that K appears to be a good, or nearly good, quantum number.

The three electron-spin wave functions for T_1 each have a different symmetry, Γ_{es}: A_2, B_1, and B_2. When first order spin–orbit coupling is the dominant mechanism in intersystem crossing, the angular momentum selection rules are given by, using the notation in Hund's case (b), by

$$\Delta S = \pm 1; \quad \Delta J = 0; \quad \Delta N = 0, \pm 1;$$
$$\Delta K = K - K' = 0; \quad + \leftrightarrow +, - \leftrightarrow -. \tag{9}$$

This case is possible for $S_0 \leftrightarrow T_1(\Gamma_{es} = A_2)$ only. It is likely that second or higher order intersystem crossing through spin–orbit vibronic coupling or spin–orbit rotational coupling is important. Here all three triplet spin functions may be allowed and the corresponding selection rules are given by[41]

$$\Delta S = \pm 1; \quad \Delta J = 0; \quad \Delta N = 0, \pm 1;$$
$$\Delta K = K - K' = 0, \pm 1, \pm 2; \quad + \leftrightarrow +, - \leftrightarrow -. \tag{10}$$

These selection rules and corresponding symmetries apply equally for motion through the transition state. Since the coupling mechanism(s) for intersystem crossing is not known, the number of spin states g_t paired with each vibrational level at the transition state is not known ($g_t = 1$, 2, or 3).

3. Nuclear spin statistics

Nuclear spin statistics have important experimental consequences for ketene. In CH_2CO, hydrogen atoms have a nuclear spin of 1/2. Four nuclear spin wave functions generate the representation, $\Gamma_{ns} = 3A_1 \oplus B_2$ in C_{2v}, where the three A_1 states correspond to $I = 1$ (*ortho*) nuclear spin states and the B_2 state is the $I = 0$ (*para*) state. Since hydrogen nuclei are *fermions*, symmetry operations which exchange them must change the sign of the wave function. Thus the symmetry class of the total wave function for the eigenstate, Γ, must be either B_1 or B_2. Therefore, since the vibronic symmetry of CH_2CO in the ground state is A_1, only b_1 (K''_a = odd, K''_c = odd) or b_2 (K''_a = odd, K''_c = even) rotational states can combine with *ortho* ($I = 1$) states while a_1 (K''_a = even, K''_c = even) or a_2 (K''_a = even, K''_c = odd) rotational states combine with *para* ($I = 0$) state.

For the case of CD_2CO, deuterons have a spin of 1 and each deuteron can have three different nuclear spin wave functions. Hence nine nuclear spin wave functions are generated for CD_2CO and give the representation, $\Gamma_{ns} = 6A_1 \oplus 3B_2$, where five A_1 states correspond to the quintet ($I = 2$) functions, one A_1 state is the singlet ($I = 0$) function, and three B_2 states are the triplet ($I = 1$) functions. Since deuterons are *bosons*, Γ must be A_1 or A_2. Therefore, in the ground state CD_2CO (A_1 vibronic symmetry), only a_1 (K''_a = even, K''_c = even) or a_2 (K''_a = even, K''_c = odd) rotational states combine with *ortho* ($I = 2, 0$) states, while b_1 (K''_a = odd, K''_c = odd) or b_2 (K''_a = odd, K''_c = even) rotational states can combine with *para* ($I = 1$) states. For CD_2CO, the *ortho* ($I = 0, 2$) states combine with K''_a = even and the *para* ($I = 1$) states combine with K''_a = odd, opposite to the case for CH_2CO. Nuclear spin statistical weights for CH_2CO are 3 for *ortho* and 1 for *para*, while for CD_2CO they are 6 for *ortho* and 3 for *para*.

It should be noted that the nuclear spin wave function and statistical weight are unchanged by UV excitation and/or radiationless transition. Thus for states reached by perpendicular dipole (b_1, b_2) transitions from the ground vibronic state, K_a even and odd are reversed (e.g., for CH_2CO $S_1 K_a$ even corresponds to *ortho*). This is especially important near the thresholds for rovibrational energy levels at the transition state. Nuclear spin is not cooled in the jet expansion and so the degeneracies, relative populations at room temperature, control the weights of *ortho* and *para* species.

As the molecule passes through the transition state to products, the symmetry of the wave function and the other conserved quantities established during excitation are un-

TABLE I. The scaled *ab initio* vibrational frequencies for the C_s^{II} transition states of CH$_2$CO and CD$_2$CO.

	CH$_2$CO[a]	CD$_2$CO[b]
$\nu_1^{\ddagger}(a')$ asym C–H(D) stretch	3178	2380 (2573)
$\nu_2^{\ddagger}(a')$ sym C–H(D) stretch	2997	2150 (2314)
$\nu_3^{\ddagger}(a')$ C–O stretch	2029	2029 (2153)
$\nu_4^{\ddagger}(a')$ CH(D)$_2$ scissor	1183	874 (930)
$\nu_5^{\ddagger}(a')$ CH(D)$_2$ rock	472	383 (406)
$\nu_6^{\ddagger}(a')$ C–C stretch	523i	514i (550i)
$\nu_7^{\ddagger}(a')$ C–C–O bend	252	224 (232)
$\nu_8^{\ddagger}(a'')$ CH(D)$_2$ wag	366	276 (283)
$\nu_9^{\ddagger}(a'')$ H(D)–C–C–O torsion	154	126 (127)

[a]Taken from Ref. 38.
[b]Frequencies in parentheses are unscaled vibrational frequencies calculated by normal-mode analysis using *ab initio* force constants of CH$_2$CO. The same scale factors as used for CH$_2$CO are multiplied to give the values without parentheses.

changed. Furthermore, some quantities not rigorously conserved may be approximate constants of the motion or nearly good quantum numbers.

C. *Ab initio* transition state structure

1. Structure and vibrational frequencies

An *ab initio* calculation has been performed by Allen and Schaefer, III[38] for the (C_s^{II}) in-plane bent $^3A''$ CH$_2$CO→CH$_2$ ($^3B_1$)+CO ($^1\Sigma^+$) and the (C_s^{I}) out-of-plane bent $^3A'$ CH$_2$CO→CH$_2$ ($^3B_1$)+CO ($^1\Sigma^+$) dissociation paths. The C_s^{II} stationary point for $^3A''$ ketene dissociation has been found to be a true transition state. The C_s^{I} stationary point for $^3A'$ ketene dissociation is the potential energy maximum along the torsional or internal rotational coordinate of the C_s^{II} transition state. The barrier to internal rotation is calculated to be 384 cm^{-1} and is expected to be significantly less.[38]

The *ab initio* (DZP CISD, double-zeta basis with polarization–configuration interaction with singles and doubles) values for transition-state vibrational frequencies, which have been scaled in Ref. 38 by multiplying by the ratio of experimental to *ab initio* values for ground state ketene vibrational frequencies, are listed in Table I. Vibrational frequencies for the C_s^{II} transition state of CD$_2$CO are calculated by normal-mode analysis using the *ab initio* force constants of CH$_2$CO, scaled as for CH$_2$CO, and listed in Table I. The corresponding zero-point energies are given in Table II. The scaled harmonic vibrational frequencies obtained from quadratic force constants are 154 cm^{-1} for

TABLE II. The zero-point vibrational energies of ketene and methylene.[a]

	CH$_2$CO	CD$_2$CO
$S_0(^1A_1)$[b]	6712	5556
TS[c]	5295	4204
^{3}CH(D)$_2$ fragment[d]	3495	2609

[a]The unit is cm^{-1}.
[b]Calculated from the values in Ref. 51.
[c]Calculated from the scaled *ab initio* vibrational frequencies for $\nu_1^{\ddagger}-\nu_8^{\ddagger}$; $\nu_9^{\ddagger}$ is from Table IV.
[d]Calculated from the values in Ref. 56.

H–C–C–O torsion, 252 cm^{-1} for C–C–O bending, and 366 cm^{-1} for CH$_2$ wagging for the CH$_2$CO transition state. The distinct steps in $k(E)$ are observed in the first 200–300 cm^{-1} above threshold, and are most likely to be associated with these low-frequency vibrational modes.

2. Hindered internal rotation

The torsional degree of freedom cannot be treated as an isolated harmonic vibration because the top of the barrier to internal rotation about the C–C bond is of the same order as the energy range of interest. The *ab initio* values for the barrier to internal rotation are 436 (CISD level) or 384 with Davidson correction cm^{-1}.[38] Furthermore, the internal rotation and the solid body rotation about the same axis are significantly coupled. Thus the Schrödinger's equation for at least these two coupled degrees of freedom must be treated in detail.

The potential energy for the internal rotation is approximated as a cosine series[42]

$$V(\theta) = (V_0/2)[1-\cos(2\theta)] + (V_1/2)[1-\cos(4\theta)] + \cdots, \tag{11}$$

where V_0 is the barrier height, V_1 changes the shape of the potential function, and θ is the dihedral angle between the CH$_2$ and CCO planes. The *ab initio* C_s^{II} transition-state structure is used for the evaluation of moments of inertia for both CH$_2$CO and CD$_2$CO. The moment of inertia of the CH$_2$ "top" about the C–C bond, I_{top}, is 1.88 amu Å^2 while that of the CO "frame", I_{frame}, is 16.9 amu Å^2 for CH$_2$CO. For this case, where $I_{frame}>I_{top}$, it is convenient to use the principal axes of the whole molecule as the coordinate system.[43] For an asymmetric top with a single twofold internal rotor, the Hamiltonian can be written as[44,45]

$$H = H_{rot} + F(p-P)^2 + V(\theta). \tag{12}$$

Here, H_{rot} is the standard rigid-rotor asymmetric-top rotational Hamiltonian and F is the effective rotational constant for the internal rotation of the top about its symmetry axis

$$F = \frac{h^2}{8\pi^2 r I_{top}}; \quad r = 1 - \sum_g \frac{\lambda_g I_{top}}{I_g}, \quad g=(a,b,c). \tag{13}$$

Here, I_{top} is the moment of inertia of the top about the symmetry axis, (I_a,I_b,I_c) are the principal moments of inertia of the whole molecule, and $(\lambda_a,\lambda_b,\lambda_c)$ are the direction cosines of the symmetry axis of the top to the principal axes. Since there is a plane of symmetry, λ_c vanishes. The momenta P and p are defined as

$$P = \sum_i P_i\hat{i}; \quad P_i = \frac{\partial T}{\partial \omega_i}, \quad (i=a,b,c); \quad p = \frac{\partial T}{\partial \dot{\theta}}, \tag{14}$$

where $T=(H-V)$ and ω_i is the angular velocity about axis i. In the second term in Eq. (12), $(p-P)$ represents the relative angular momentum of the top and the frame. The Hamiltonian in Eq. (12) can be rewritten as

$$H = A^{\ddagger'}P_a^2 + B^{\ddagger'}P_b^2 + C^{\ddagger}P_c^2 - 2F(\alpha P_a p + \beta P_b p)$$
$$+ F\alpha\beta(P_a P_b + P_b P_a) + Fp^2 + V(\theta), \tag{15}$$

TABLE III. Molecular parameters used in the calculation of hindered internal rotation energy levels of the transition state.

Parameters[a]	CH_2CO	CD_2CO
I_a	6.74	8.59
I_b	62.9	71.0
I_c	69.6	79.6
λ_a	0.95	0.95
λ_b	0.31	0.31
F	12.1	7.56
I_{top}	1.88	3.76
$A^{\ddagger'}$	3.35	3.26
$B^{\ddagger'}$	0.268	0.237
$C^\ddagger$	0.242	0.212

[a]The units are amu Å^2 for I_x ($x=a,b,c$, top) and cm^{-1} for F, $A^\ddagger$, $B^\ddagger$, and $C^\ddagger$ (see Sec. IV C 2 for definitions). The *ab initio* (DZP CISD level calculation) C_s^{II} transition-state structure is used for both CH_2CO and CD_2CO (Ref. 38).

where

$$A^{\ddagger'}=A^\ddagger+F\alpha^2, \quad B^{\ddagger'}=B^\ddagger+F\beta^2,$$

$$\alpha=\frac{\lambda_a I_{top}}{I_a}, \quad \beta=\frac{\lambda_b I_{top}}{I_b} \tag{16}$$

and $\ddagger$ denotes the transition-state geometry.

The Hamiltonian matrix can be set up using the symmetric-prolate-top, free-rotor basis set. The nonvanishing elements of the Hamiltonian matrix are given in Ref. 45. The matrix elements off-diagonal in $K^\ddagger$ are very small for the nearly symmetric-top ketene molecule at its transition state ($\beta\approx0.0092$, $(B^{\ddagger'} - C^\ddagger)\approx0.026$ cm^{-1} for CH_2CO), and $K^\ddagger$ splitting is not expected to be observed with the resolution of features in this work. Thus the matrix elements off-diagonal in $K^\ddagger$ are neglected in the calculation. The matrix elements in the free-rotor basis set, $|m\rangle=(2\pi)^{-1/2}\exp(-im\theta)$ are thus

$$\langle m|H|m\rangle=Fm^2-2F\alpha K^\ddagger m+(V_0/2)+(V_1/2), \tag{17}$$

$$\langle m|H|m\pm2\rangle=-V_0/4, \tag{18}$$

$$\langle m|H|m\pm4\rangle=-V_1/4. \tag{19}$$

Here, the diagonal matrix element term of $(-2F\alpha K^\ddagger m)$ arises from the coupling of internal rotation and overall rotation. The effective rotational constants about the principal axes have been modified due to the effect of internal rotation. The energy levels for hindered internal rotation for each value of $K^\ddagger$ are calculated by diagonalizing the above Hamiltonian matrix. The rovibrational energy levels are calculated by adding the symmetric top approximation for the rotational energies using $(A^{\ddagger'}, B^{\ddagger'}, C^\ddagger)$ as rotational constants. A 40×40 Hamiltonian matrix is diagonalized to give the eigenvalues. All parameters used in the calculation are listed in Table III.

Energy levels are calculated numerically for a wide range of V_0 and V_1 for comparison to the thresholds in the measured rate constants. Table IV shows energy levels with nuclear spin statistical weights for hindered rotor states for $K^\ddagger=0$, 1, 2 for CH_2CO and CD_2CO transition states with

TABLE IV. The energy and nuclear spin of hindered internal rotor states for different $K^\ddagger$ for the CH_2CO and CD_2CO transition states.[a]

	CH_2CO			CD_2CO		
m	$K^\ddagger=0$	$K^\ddagger=1$	$K^\ddagger=2$	$K^\ddagger=0$	$K^\ddagger=1$	$K^\ddagger=2$
0	0	(−1)	−2	(0)	−1	(−3)
−1	(0)	−1	(−2)	0	(−1)	−3
+1	(99)	99	(99)	84	(83)	81
−2	103	(102)	99	(84)	83	(81)
+2	164	(166)	170	(149)	150	(146)
−3	(189)	181	(172)	155	(151)	151
+3	(209)	218	(231)	190	(195)	188
−4	276	(253)	236	(216)	201	(209)
+4	278	(301)	321	(225)	244	(228)
−5	(383)	351	(327)	283	(254)	268
+5	(383)	414	(439)	284	(313)	292
−6	514	(476)	447	(363)	327	(345)
+6	514	(552)	583	(363)	400	(375)

[a]The energy levels are in cm^{-1} for $V_0=240$, $V_1=20$ cm^{-1} for both CH_2CO and CD_2CO. The energy values in parentheses are *ortho* states and those without parentheses are *para* states. The symmetric rotor energy term values for $(N,K^\ddagger)$ states are not included. The energy values listed in each column are those with respect to the corresponding zero-point energy levels for $K^\ddagger=0$, 57 and 46 cm^{-1} for CH_2CO and CD_2CO, respectively.

$V_0=240$ cm^{-1} and $V_1=20$ cm^{-1}. The hindered rotor energy levels coupled to each $K^\ddagger$ are listed with respect to the zero-point energy at $K^\ddagger=0$. The shift of the zero-point energies with increasing $K^\ddagger$ due to the coupling of the hindered internal rotation to the overall rotation is less than 4 cm^{-1}, as shown in Table IV.

D. RRKM theory

The RRKM rate constant for unimolecular reaction of ketene for the case of complete K mixing ($K=-J$ to J) in the highly excited molecule can be calculated as follows:[46]

$$k[E,J\leftarrow(J'',K''),\Gamma_{ns}]$$

$$=\frac{g_t\Sigma_{K^\ddagger=-N^\ddagger}^{N^\ddagger}\Sigma_n P(E+E_{thermal}-\varepsilon_{n,N,K^\ddagger,\Gamma_{ns}}^\ddagger)}{\Sigma_{K=-J}^J h\rho(E+E_{thermal}-W_{J,K,\Gamma_{ns}})}, \tag{20}$$

$$\varepsilon_{n,N^\ddagger,K^\ddagger,\Gamma_{ns}}^\ddagger=E_{th}+W_{N^\ddagger,K^\ddagger}^\ddagger+\sum_{i=1}^{s-1} h\nu_i^\ddagger\left(n_i+\frac{1}{2}\right), \tag{21}$$

$$W_{N^\ddagger,K^\ddagger}^\ddagger=\tfrac{1}{2}(B^\ddagger+C^\ddagger)[N^\ddagger(N^\ddagger+1)-K^{\ddagger2}]+A^\ddagger K^{\ddagger2}, \tag{22}$$

$$W_{J,K}=\tfrac{1}{2}(B+C)[J(J+1)-K^2]+AK^2, \tag{23}$$

$$E_{thermal}=\tfrac{1}{2}(B+C)[J''(J''+1)-K''^2]+AK''^2. \tag{24}$$

Here rotational energies are approximated by those of a symmetric top with K replacing K_a for ketene. Since even and odd parity states are almost equally populated in reactants and transition states,[34] states with both parities are counted in both the numerator and denominator of Eq. (5). In Eq. (20), rovibronic states which are symmetry allowed with a nuclear spin state represented by Γ_{ns} are counted in both numerator and denominator of Eq. (5). E is the photolysis photon energy and $E_{thermal}$ is the thermal rotational energy of the parent molecule in the pulsed molecular jet for the (J'',K'') level. J

TABLE V. The parameters used in the RRKM fits to experimental results.[a]

	CH$_2$CO	CD$_2$CO
$A^{\ddagger}$	2.50 cm^{-1}	1.96 cm^{-1}
$B^{\ddagger}$	0.268 cm^{-1}	0.237 cm^{-1}
$C^{\ddagger}$	0.242 cm^{-1}	0.212 cm^{-1}
T_{rot}	4 K	4 K
E_{th}	28 250 (10) cm^{-1}	28 310 (15) cm^{-1}
ν_{im}[b]	100 (40)i cm^{-1}	⋯
f/g_t[c]	1.11 (0.11)	1.19 (0.07)
V_0	240 (30) cm^{-1}	240 (30) cm^{-1}
V_1	20 (20) cm^{-1}	20 (20) cm^{-1}
$\nu_7^{\ddagger}$ (C–C–O bend)	250 (15) cm^{-1}	[d]185 (20) cm^{-1}
$\nu_8^{\ddagger}$ (CH(D)$_2$ wag)	290 (15) cm^{-1}	[d]240 (20) cm^{-1}

[a]The values in parentheses are uncertainties obtained from the fits.

[b]The imaginary frequency (ν_{im}) is used only for the fit to the first step in $k(E)$ for CH$_2$CO dissociation.

[c]$\rho(E) = \rho_{WR}(E) \times f$; $\rho(E)$ is used for the RRKM fits. The $\rho_{WR}(E)$ is the density of vibrational states of the reactant calculated from the Whitten–Rabinovitch approximation; $\rho_{WR}(E) = 1.36 \times 10^4$ (/cm^{-1}) for CH$_2$CO(S_0) and 4.78×10^4 (/cm^{-1}) for CD$_2$CO(S_0) at $E = 28\ 500$ cm^{-1}.

[d]Assignments are tentative (see the text).

is the angular momentum of the excited state of ketene and $W_{J,K}$ its rotational energy. $N^{\ddagger}$ is the rotational angular momentum of ketene at the transition state on the T_1 surface and $W_{N^{\ddagger},K^{\ddagger}}^{\ddagger}$ the rotational energy. E_{th} is the reaction threshold, the difference between zero-point energies of the ground state reactant (S_0) and transition state on the T_1 surface. The number of vibrational degrees of freedom of the stable molecule, s, is 9 for ketene and n represents the set of eight vibrational quantum numbers for the transition state. The electron spin multiplicity is approximated by multiplying the number of vibrational states of the transition state by g_t. This approximation is made by setting $N^{\ddagger} = J^{\ddagger}$ rather than summing $N^{\ddagger}$ over $J^{\ddagger} - 1$, $J^{\ddagger}$, and $J^{\ddagger} + 1$. In the case where all three electron spin states are strongly coupled $g_t = 3$.

Ketene in the ground state is a near-prolate asymmetric top ($\kappa = -0.997$).[47] The symmetric top approximation is used for the calculation of rotational energy levels for both reactants and transition state. The K and $K^{\ddagger}$ in the symmetric top approximation are the projections of the rotational angular momentum, $\mathbf{N}$ ($\mathbf{J} = \mathbf{N} + \mathbf{S}$), on the molecule-fixed a axis for the molecule in the excited reactant state and the transition state, respectively. The rotational constants of UV-excited ketene molecules are assumed to be the same as those (A, B, C) in the ground state. $A^{\ddagger}$, $B^{\ddagger}$, and $C^{\ddagger}$ are the rotational constants for the transition state as calculated from the *ab initio* structure, Table V.[38] These rotational constants for the transition state are modified due to the strong coupling of the hindered internal rotation to the overall rotation of the molecule (See Sec. IV C 2).

$P(E_1)$ is the transmission probability for each quantized reaction threshold of the transition state. Classically, the transmission probability is the step function, $h(E_1)$

$$h(E_1) = 0, \quad E_1 < 0,$$
$$= 1, \quad E_1 > 0. \tag{25}$$

Quantum mechanically, $P(E_1)$ can be calculated for one-dimensional tunneling through the reaction barrier along the reaction coordinate. Formulas for $P(E_1)$ (Ref. 46) for inverted parabolic or Eckart barriers[48,49] give about the same results.[31] The inverted parabolic function is used here.

The density of reactant states, $\rho(E) = f\rho_{WR}(E)$, is taken to be a constant f multiplied by the harmonic oscillator density calculated using the Whitten–Rabinovitch (WR) approximation[50]

$$\rho_{WR}(E, J = 0) = \frac{(E + E_{zp})^{s-1}}{(s-1)! \Pi_{i=1}^{s} \nu_i}. \tag{26}$$

Here E_{zp} is the zero-point energy of the ketene molecule and ν_i is the ith fundamental vibrational frequency of S_0 ketene taken from Ref. 51. The contributions of $\rho(S_1)$ and $\rho(T_1)$ to ρ_{total} are less than 1% and are neglected. In Eq. (20), the density of vibrational states for each nuclear spin state, $\rho(E, \Gamma_{ns})$, is approximated as half of the total vibrational states, $\rho(E, \Gamma_{ns}) = [\rho(E)/2]$ (Refs. 27 and 52) and the sum over K is made over all $2J + 1$ values.

An experimental CO (v, J) product rise curve is the sum of CO product rise curves for different initial quantum states of ground state ketene and the different optical transitions for each. The measured rate constant, k_{obs}, is obtained from a single exponential fit to the experimental CO product rise curve which is in reality a multiexponential one. This is equivalent to the mean reaction time rate constant,[31] and has been found to give an accurate value for the true average rate constant.[53,54]

The population of a (J, K') level in the S_1 state is determined by the product of the Hönl–London factor and the initial population of (J'', K'') states of ketene in the ground state prepared in the supersonic jet. Nuclear spin is found not to be cooled down in the molecular jet.[27] Initial (J'', K'') states of ketene are otherwise populated according to a Boltzmann distribution for a rotational temperature of 4 K. When K is assumed to be completely mixed for highly vibrationally excited S_0, as Eq. (20) implies, the population of K states is determined by J. When K is assumed to be conserved, its value at the transition state depends on which couplings are responsible for intersystem crossing. Since the coupling strengths are not known, calculations were done for one of the least restrictive possibilities, $K^{\ddagger} = K'$, $K' \pm 2$, and $K' \pm 4$ where K' is taken as $K'' \pm 1$. Calculations made with more restrictive selection rules were not sensibly different.

The angular momentum (J) distribution of the excited reactant states from parallel (A-type) or perpendicular (B-, C-type) transitions are identical within one unit of angular momentum, and therefore RRKM fits are not sensitive to the type of transition. The line strengths for a perpendicular transition are used. The rate constants are calculated for each angular momentum (J), and averaged over the distribution of $J = J''$, $J'' \pm 1$ in the reactant states. The rate constants for each nuclear spin state, thermally populated J'', K'' state, and allowed value of J are calculated separately and averaged using the proper nuclear spin statistical weights as follows:
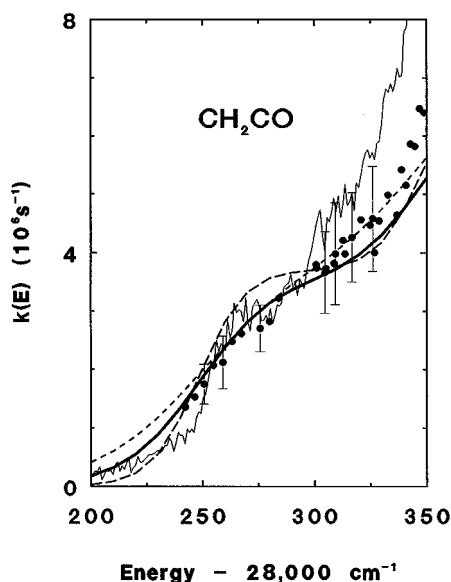
FIG. 11. Rate constants (filled circles) and $CO(v=0, J=12)$ PHOFEX curve taken at 50 ns delay time are shown with RRKM fits for CH_2CO dissociation in the reaction threshold region. The solid line is the RRKM fit when the threshold energy is 28 250 cm^{-1} and $\nu_{im}=100i$ cm^{-1}. The RRKM fits for $\nu_{im}=60i$ cm^{-1} (long dashes) and $\nu_{im}=140i$ cm^{-1} (short dashes) are shown for the same threshold energy. The PHOFEX intensity is arbitrarily scaled for comparison with the rate constants.

$$k(E)=\sum_{\Gamma_{ns}} P(\Gamma_{ns}) \sum_{J'',K''} N(J'',K'',\Gamma_{ns})$$

$$\times \sum_{J} P[J\leftarrow(J'',K''),\Gamma_{ns}]k[E,J\leftarrow(J'',K''),\Gamma_{ns}].$$
(27)

Here $P(\Gamma_{ns})$ is the statistical weight for Γ_{ns} normalized to unity, $N(J'',K'',\Gamma_{ns})$ is the thermal rotational distribution of ketene for Γ_{ns} (zero for either even or odd K''), and $P[J\leftarrow(J'',K''),\Gamma_{ns}]$ is the probability for a transition to J from an initial state (J'',K'') for each Γ_{ns} state.

E. RRKM fits

The RRKM formalism above may be used to extract information on transition-state energy levels and structure and on the density of reactant states from the steplike structures in the rate constants and PHOFEX spectra. Since there are many more distinguishable features in the data than fitting parameters, the comparison also tests the validity of the model.

1. Reaction threshold

For CH_2CO dissociation, the first sharp step in $k(E)$ accurately defines the reaction threshold energy. It is reproduced well by RRKM calculations for a threshold energy, $E_{th}=28\,250\pm10$ cm^{-1} and an imaginary frequency, $\nu_{im}=(100\pm40)i$ cm^{-1}, Fig. 11. The singlet-triplet splitting of CH_2, Δ_{ST}, has been measured to be 3147 ± 5 cm^{-1}.[55] The singlet threshold energy for CH_2CO dissociation has been accurately measured from $^1CH_2$ PHOFEX spectra,
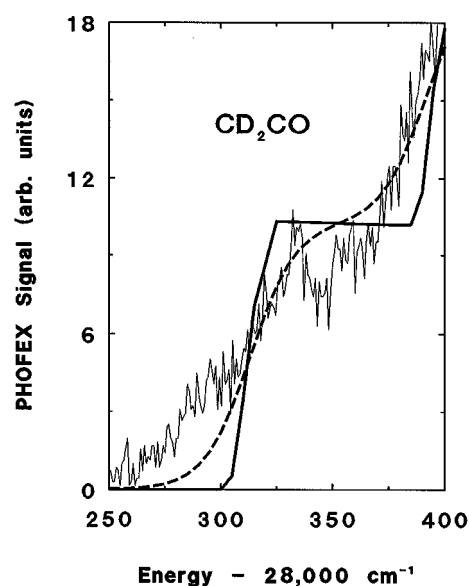

FIG. 12. The $CO(v=0, J=12)$ PHOFEX curve taken at 1.7 μs reaction time is shown with RRKM fits for the CD_2CO dissociation in the reaction threshold region. The solid line is the RRKM fit when the threshold energy is 28 310 cm^{-1} without tunneling correction. The dashed line is the RRKM fit when $\nu_{im}=60i$ cm^{-1}.

$E_{th}(singlet)=30\,116.2\pm0.4$ cm^{-1}.[27] Therefore, the reaction barrier relative to the products, E_b is determined by

$$E_b=[\Delta_{ST}-\{E_{th}(singlet)$$
$$-E_{th}(triplet)\}]=1281\pm15 \text{ cm}^{-1}$$
(28)

or 3.66 ± 0.05 kcal/mol. This is about 40% less than the *ab initio* calculation of 5.8 kcal/mol.[38]

For CD_2CO dissociation, $k(E)$ could not be measured in the reaction threshold region (*vide supra*); however, the first distinct step in the PHOFEX spectrum for $CO(v=0, J=12)$, Fig. 12, gives the reaction threshold energy as $28\,310\pm15$ cm^{-1}. The solid line in Fig. 12 is the RRKM rate constant calculated without tunneling. The zero-point energies of the normal and deuterated ketene and triplet methylene molecules are calculated using the spectroscopic and theoretical results, respectively, and listed in Table II.[51,56] The barrier height relative to products, E'_b, is given by

$$E'_b=E_b+ZPE(^3CH_2-^3CD_2)$$
$$-[E_{th}+ZPE(CH_2CO-CD_2CO)-E'_{th}]$$
$$=1071\pm40 \text{ cm}^{-1}.$$
(29)

Here $ZPE(^3CH_2-^3CD_2)$ is the difference of zero-point energies between $^3CH_2$ and $^3CD_2$ fragments, 886 cm^{-1},[56] and $ZPE(CH_2CO-CD_2CO)$ is the difference of zero-point energies between the ground states of CH_2CO and CD_2CO, 1156 cm^{-1}.[51] The reaction barrier is thus 1071 ± 40 cm^{-1} (3.06 ± 0.10 kcal/mol). The difference in ZPE's between CH_2CO and CD_2CO at their T_1 transition states is $[E_{th}-E'_{th}+ZPE(CH_2CO-CD_2CO)}]=1096\pm20$ cm^{-1}, Fig.
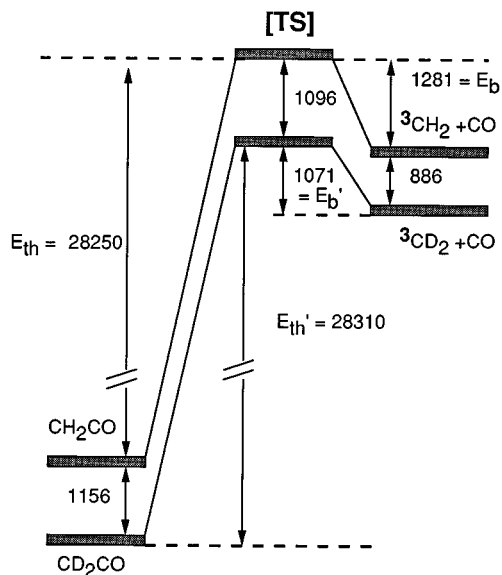
FIG. 13. Energy diagram for the dissociation of CH_2CO and CD_2CO on the triplet surface. The energy differences (cm^{-1}) among the zero-point energy levels are shown (uncertainties in text).

13. The *ab initio* difference using Table IV for torsion and harmonic, scaled values from Table I for the remaining seven frequencies is 1091 cm^{-1}.

2. Hindered internal rotor levels at the transition state

The step structures in the measured $k(E)$ and $J_{CO}=12$ PHOFEX spectra exhibit the same shapes in the first 200 cm^{-1} above threshold. The *ab initio* predictions of vibrational frequencies, Table I, indicate that the torsion or internal rotation degree of freedom is responsible for the vibrational structure closest to threshold. The barrier height V_0 of the potential, as defined in Eq. (11) and shown in Fig. 14, is chosen to fit the first energy spacing in CH_2CO. The level
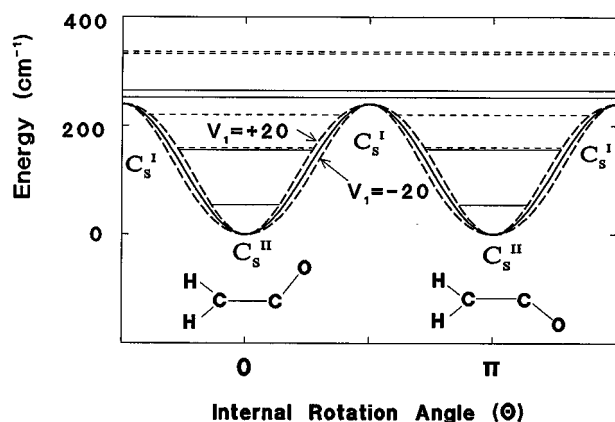

FIG. 14. The model potential function for the hindered internal rotor, $V(\theta)=(1/2)V_0(1-\cos 2\theta)+(1/2)V_1(1-\cos 4\theta)$, where $V_0=240$ cm^{-1} and $V_1=0$ (solid line) and ± 20 cm^{-1}. The *ab initio* C_s^{II} transition-state geometry is drawn. For $C_s^I O$ is out of the plane with the CCO plane bisecting the HCH angle. The calculated energy levels listed in Table IV are shown for $K=0$.

positions were not strongly sensitive to V_1 in the range 20 ± 20 cm^{-1} and no improved fit could be found for values outside of this range. The fit to the position and amplitude of higher levels, Fig. 6, indicates that the basic form of the potential and the symmetries and degeneracies of the levels are correct. Some caution must be exercised since the features observed at 28 390 and 28 450 cm^{-1} correspond to energy levels calculated for $m=+2$ and -3 at 28 407 and 28 432 cm^{-1}. The splitting between these states just at the top of the barrier to internal rotation should be particularly sensitive to the barrier shape and may therefore be incorrectly predicted. Since the nuclear spin state symmetry is conserved, the threshold photon energies for *para* states of CH_2CO at the transition state are those shown in Table IV and for *ortho* states are lower by ≈ 9.7 cm^{-1}. For CD_2CO, since *ortho* states ($K''=0$) lie below *para* states ($K''=1$) in the ground state, threshold energies for *para* rovibrational states should be ≈ 5.0 cm^{-1} (energy difference between 1_{10} and 0_{00} states) lower than the energy term values listed in Table IV, while those for *ortho* states are as listed. The excellent fit to CD_2CO, Fig. 7, using the potential for CH_2CO indicates that the vibration is correctly identified and that the reduced mass of the motion is correctly formulated.

3. Bending vibrations of the transition state

The *ab initio* frequencies of the three bending vibrations which become free rotations in the products make them all candidates for influencing $k(E)$ in the range 200–400 cm^{-1} above threshold. Unfortunately, the features in $k(E)$ are much less distinct in this energy range than closer to threshold. Fortunately, PHOFEX spectroscopy provides a means to search for molecules coming through the transition state with specific vibrations excited. This is because the product energy state distribution is determined by the positions and momenta of each atom as it passes through the transition state as well as by the potential in the exit valley.[30] That $P(E,v=0,J_{CO})$ peaks at $J_{CO}=12$ near threshold has confirmed the *ab initio* CCO angle of 116°.[30,38] The *ab initio* values for the geometry and vibrational frequencies at the transition state reproduce the Gaussian shape of the observed distributions quite well, Fig. 3 and Ref. 30. The C–C–O bending mode is the largest contributor to the width of the CO rotational distribution.[30] The scaled *ab initio* frequency for C–C–O bending is 252 cm^{-1}, and a noticeable change of CO rotational distribution is expected to occur when the first quantum of C–C–O bending is energetically accessible at the transition state. In the harmonic oscillator approximation, the momentum distribution resulting from the node in the first excited state of the C–C–O bend is a bimodal Gaussian function. The distribution of CO angular momentum transferred from C–C–O bending motion for $v=1$ is given by

$$P_1(J_\perp)=\frac{2}{\sqrt{\pi}(\Delta J_{\perp 1})^3}J_\perp^2\exp\left[-\frac{(J_\perp)^2}{(\Delta J_{\perp 1})^2}\right], \quad (30)$$

where $J_\perp$ is the CO angular momentum along the c axis and $\Delta J_{\perp 1}$ is the width of the distribution calculated from the classically allowed maximum linear momenta of C and O atoms for $v=1$. The $P_1(J_\perp)$ is convoluted with the CO an-
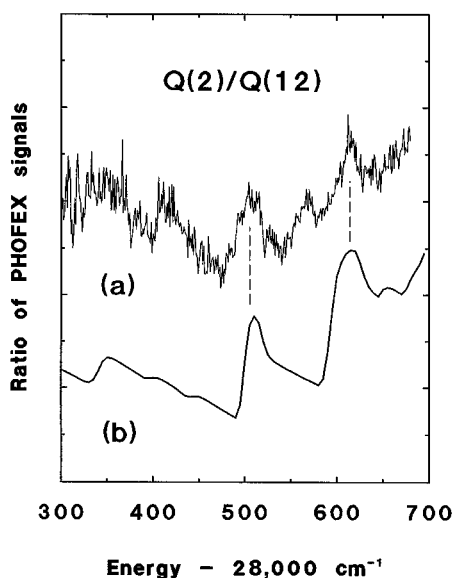
FIG. 15. Ratio of the populations of CO($v=0$, $J=2$) to CO($v=0$, $J=12$), $P(E,v=0,J_{CO}=2)/P(E,v=0,J_{CO}=12)$ for CH$_2$CO. (a) From the ratio of the $J=2$ and $J=12$ PHOFEX curves in Fig. 8. (b) The calculated ratio of the yields of CO($J=2$) to CO($J=12$) products using the model described in Sec. IV E 3 for a C–C–O bending frequency of 250 cm^{-1}. The ratio of the maximum and minimum points on curves (a) and (b) are 1.80 and 1.90, respectively.
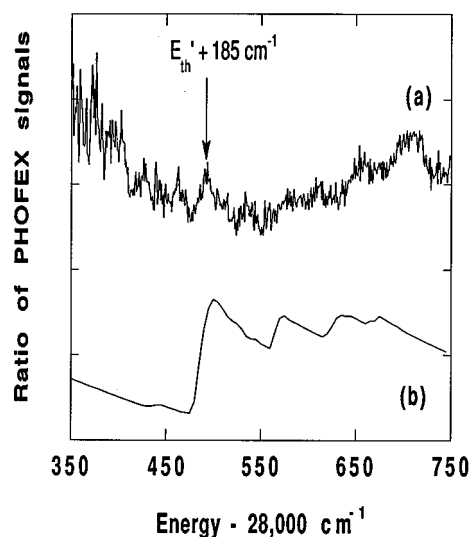

FIG. 16. The ratio of the $J=2$ and $J=12$ CD$_2$CO PHOFEX curves in Fig. 9. Curves as in Fig. 15 with the ratios for curves (a) and (b) being 2.13 (or 1.62 if 28 700 cm^{-1} is used) and 2.22, respectively.

gular momentum transferred from the motions of other vibrations to give the spread in CO angular momentum for dissociation via an individual vibrational level at the transition state. A distinct widening of the CO rotational distribution about the peak at $J_{CO}=12$ imposed by the forces in the exit valley is expected when the molecule passes through the first excited C–C–O bending level of the transition state. The peaks in Fig. 8, curve (c) and the change in slope of curve (a) are a clear illustration.

The overall CO rotational distribution for a given photon energy, E, is calculated by summing the distributions for each vibrational level at the transition state multiplied by the corresponding statistical weight for each vibrational state. All energetically accessible vibrational levels of the transition state are assumed to be equally probable. Table IV is used for the vibrational frequencies of hindered internal rotation. The yields of CO($v=0$, $J=2$), $P(E,v=0,J_{CO}=2)$, and of CO($v=0$, $J=12$), $P(E,v=0,J_{CO}=12)$, are calculated as a function of the available energy and their ratios compared to the PHOFEX data from Sec. III C in Fig. 15.

The overall shape of the ratio as a function of energy is well matched by the calculation, and the sharp peaks at around 28 500 and 28 600 cm^{-1} in curve (a) are reproduced well by the calculation, curve (b), when the vibrational frequency of the C–C–O bend is 250 cm^{-1}. The first sharp peak at 28 500 cm^{-1} is assigned as the first excited C–C–O bending level and the peak at 28 600 cm^{-1} as the combination with one quantum of hindered rotation. This agrees very well with the scaled value of 252 cm^{-1} for the C–C–O bending mode.

The rate constant curve for CH$_2$CO requires a level to be

added at 290 cm^{-1}, most likely the CH$_2$ wag calculated *ab initio* at 366 cm^{-1}. For CD$_2$CO the *ab initio* CCO bending, $\nu_7^{\ddagger}$, frequency is 224 cm^{-1}.[38] The *ab initio* isotope ratio for the CH$_2$ wag, $\nu_8^{\ddagger}$(CH$_2$CO)/$\nu_8^{\ddagger}$(CD$_2$CO) = 1.33, combined with $\nu_8^{\ddagger}$(CH$_2$CO) = 290 cm^{-1} gives an estimated $\nu_8^{\ddagger}$(CD$_2$CO) = 219 cm^{-1}. This accidental resonance between $\nu_7^{\ddagger}$ and $\nu_8^{\ddagger}$ and the opportunity for coupling through internal and overall rotation about the molecular axis suggests the possibility of substantial perturbations. Inspection of Fig. 7 shows that the flattest region in the $k(E)$ curve above 28 450 cm^{-1} is 28 520–28 545 cm^{-1}, 210–235 cm^{-1} above threshold. Clearly neither $\nu_7^{\ddagger}$ nor $\nu_8^{\ddagger}$ can be in this predicted range.

For CD$_2$CO the ratio of CO($v=0$, $J=2$, $\Delta t=150$ ns) and CO($v=0$, $J=12$, $\Delta t=200$ ns) PHOFEX curves, Fig. 16, is the product of $[P(E,v=0,J_{CO}=2)/P(E,v=0,J_{CO}=12)]$ and $[\{1-\exp(-k(E)\times1.5\times10^{-7})\}/\{1-\exp(-k(E)\times2.0\times10^{-7})\}]$. The variation of the latter with E is small and the structures in the curve are mainly due to the change of relative CO(v,J) yields. A sharp peak is observed at around 28 495 cm^{-1}. As for CH$_2$CO, this suggests that the vibrational frequency for C–C–O bending of CD$_2$CO at the transition state is $\approx$(28 495–28 310=185 cm^{-1}), about 16% lower than the *ab initio* value. The peak is smaller than calculated as would be expected if the frequency were pushed down by interaction with other modes.

The rate constant curve, Fig. 7, requires an energy level to be added at 240 cm^{-1}, 21 cm^{-1} above the 219 cm^{-1} estimated from isotope ratios. The minimum in Fig. 16 at exactly this frequency does not suggest that there is much CCO bend character associated with the 240 cm^{-1} energy level. The data do not provide a convincing assignment for the 185 and 240 cm^{-1} levels.
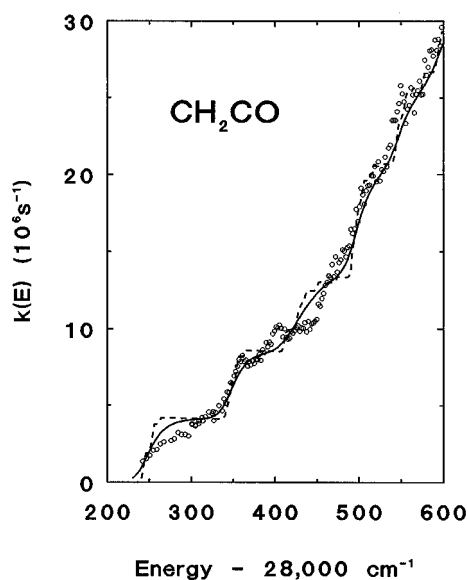
FIG. 17. The RRKM fit to CH$_2$CO dissociation rate constants. The open circles are measured rate constants. The dotted line is the RRKM fit using a step function for the transmission probability as shown in Fig. 6. The solid line is the RRKM fit including the one-dimensional tunneling with an imaginary frequency of 40i cm^{-1}. The parameters listed in Table V are used for the RRKM fits.
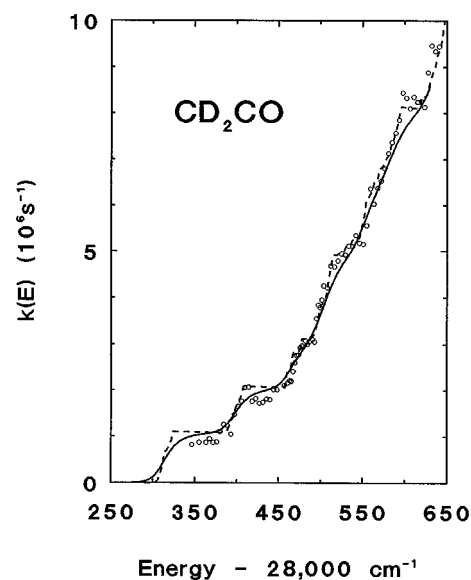
FIG. 18. The RRKM fit to rate constants of the CD$_2$CO dissociation. The open circles are measured rate constants. The dotted line is the RRKM fit using a step function for the transmission probability as shown in Fig. 7. The solid line is the RRKM fit including the one-dimensional tunneling with an imaginary frequency of 40i cm^{-1}. The parameters listed in Table V are used for the RRKM fits.

4. Density of reactant states, $\rho(E)$

The density of vibrational states of the reactant is adjusted to fit the step sizes in the $k(E)$ data of Figs. 6 and 7 to the RRKM rate with $f/g_t = 1.11$ for CH$_2$CO and 1.19 for CD$_2$CO, respectively, where $\rho(E) = f \times \rho_{WR}(E)$, as listed in Table V. The Whitten–Rabinovitch approximation predicts a 10% increase of the density of states as the energy increases from 28 250 to 28 700 cm^{-1}. This is consistent with the experiment as shown in the RRKM fits. The WR approximation gives a density of states 3.5 times higher for CD$_2$CO than for CH$_2$CO compared to 3.7 ± 0.5 to fit the rate data. For $g_t = 3$, the densities of states derived for 28 250 cm^{-1} are 4.6×10^4 (/cm^{-1}) and 1.7×10^5 (/cm^{-1}) for CH$_2$CO and CD$_2$CO, respectively. This result presumes that all three triplet spin states are fully active in the reaction. If only one or two are coupled to the S_0 levels, then the above densities must be multiplied by 1/3 or 2/3, respectively.

5. Tunneling

A much lower imaginary frequency ($100 \pm 40i$ cm^{-1}) than predicted by *ab initio* calculation ($523i$ cm^{-1}) is necessary to fit the first step in $k(E)$ for CH$_2$CO dissociation. In order to reproduce the sharp steps in $k(E)$ which are associated with vibrationally excited states of ketene at the transition state, the classical step function had to be employed. Figures 17 and 18 show that even a frequency as low as 40i smooths out the steps to a greater extent than observed. The rate and PHOFEX data actually show significant peaks in rate versus energy (e.g., 28 360 and 28 410 cm^{-1} in CH$_2$CO and 28 365 cm^{-1} in CD$_2$CO). Thus neither the classical treat-

ment nor the simple one-dimensional tunneling treatment of the reaction coordinate is satisfactory at this level of detail for these experiments.

Recently, sharp structures with pronounced peaks in $k(E)$ have been observed for intramolecular carbon atom exchange in ketene.[33] These are attributed to quantum mechanical resonances for motion along a reaction coordinate with a dip at the top of the barrier, a reaction coordinate which also involves changing contributions from at least two vibrational coordinates.[33] A quantitative understanding of the detailed step shapes must await rotationally resolved experiments, a detailed *ab initio* reinvestigation of the potential energy surface in the region of the transition state and a thorough, multidimensional quantum mechanical treatment[2–7] of the dynamics of passage through the transition state.

6. Temperature dependence of rate constants

The temperature of the jet affects the rate constants through the thermal distribution of rotational quantum numbers. At 4 K the amount of rotational energy in the ground state (2 or 3 cm^{-1}) is negligible compared to the $\sim$10 cm^{-1} resolution of features in $k(E)$. J'' values are limited to about 3 and K'' to 0 for *para* and 1 for *ortho* CH$_2$CO. In the upper state the combination of selection rules permits higher J values and K values. Since the A rotational constant is an order of magnitude larger than B or C, molecules passing through the transition state with $K^{\ddagger} = J$ must carry tens of wave numbers of energy as rotation, energy which is inaccessible to the reaction coordinate. At 4 K the calculated difference between the RRKM rate with and without K mixing is too small to be experimentally measurable. However, at 30 K where J'' val-
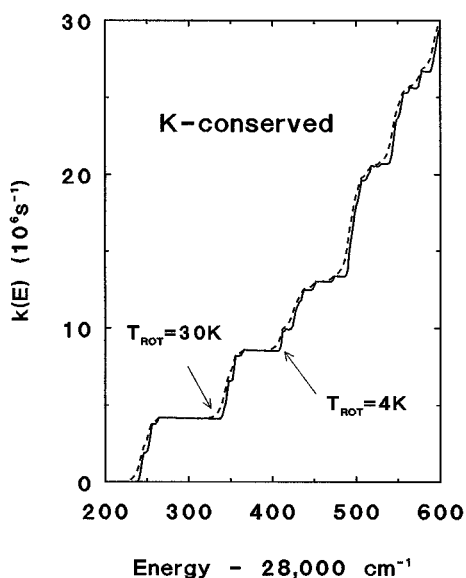
FIG. 19. RRKM calculations for CH_2CO dissociation rate constants for K conserved, $T_{rot}=4$ K (solid line) and $T_{rot}=30$ K (dashed line).

ues up to 9 are significant, the rate calculated for K mixing is much slower than that without. Figure 19 shows that with K conserved there is only a small difference between RRKM rates calculated at 4 and 30 K; while in Fig. 20 for K mixed the rate is much slower. The $CO(v=0, J=12)$ PHOFEX curves taken at 4 and 30 K are almost identical, Fig. 10. This is consistent with the RRKM calculations in Fig. 19, which implies that K quantum number is conserved in the photodissociation of ketene. A similar conclusion has been drawn from the observed density of states as a function of J for
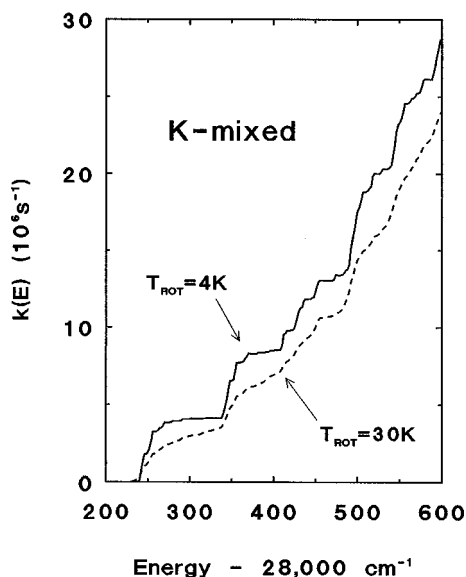

FIG. 20. RRKM calculations for CH_2CO dissociation rate constants for K mixed, $T_{rot}=4$ K (solid line) and $T_{rot}=30$ K (dashed line). The steps in the 4 K rate rise somewhat less sharply than for K conserved in Fig. 19 but are otherwise nearly identical. The 30 K rate is markedly smaller for K mixed than for K conserved.

vibrationally excited D_2CO.[15] A stronger test of K mixing will be possible with complete resolution of initial angular momentum states.

V. CONCLUSION

The stepwise increase of rate constants with increasing energy observed in ketene dissociation gives direct experimental evidence for the utility of the fundamental tenets of the RRKM theory that (1) the rate of reaction is controlled by flux through quantized transition-state thresholds, (2) the vibrational energy in the excited molecule is distributed statistically among all the vibrational degrees of freedom, and (3) the intramolecular vibrational redistribution (IVR) rate is much faster than the reaction rate. Further, and in contrast to the usual assumption in applying RRKM theory, K is seen to be a good quantum number for $J\leq 6$. The experimental observation of the quantized transition-state thresholds as distinct steps in rate constants confirms the original concept of transition-state theory that passage through the transition state is "vibrationally adiabatic" in the sense that energy is tied up in vibrational modes orthogonal to the reaction coordinate during the brief passage through the transition state region. The comparison of RRKM calculations to the experiment also supports the basic tenet of transition state theory that systems cross the transition state directly from reactants and proceed to products without recrossing. The relative step heights are quite well reproduced by RRKM calculations when unity is used for the transmission coefficient for each quantized transition state. In principle a value significantly less than unity is also possible in the unlikely circumstance that it is identical for every transition-state vibrational level threshold.

However, straightforward application of RRKM theory, even with one-dimensional tunneling along the reaction coordinate, does not reproduce the detailed shape of each step. Several steps exhibit small peaks that are clearly inconsistent with the monotonically increasing function of Eq. (20). The threshold step for the zero-point vibrational level exhibits a less rapid rise than those for excited vibrational levels. The latter rise more rapidly than could be consistent with one-dimensional tunneling for any reasonable value for the imaginary frequency for a barrier of the height observed. At this level of detail a quantum mechanical treatment of the reaction coordinate coupled to at least one other coordinate appears to be needed. Ultimately, it will be valuable to compare such a theory with rates for fully resolved initial rotational states.

The *ab initio* calculations for the geometry and vibrational frequencies of ketene at the transition state[38] have proven to be extremely useful in the interpretation of experimental results. The impulsive model calculation based on the *ab initio* transition-state geometry predicted the CO product rotational distribution quantitatively[30] thus confirming the *ab initio* CCO angle of 116°. The scaled *ab initio* value for the C–C–O bend of the CH_2CO transition state, 252 cm^{-1}, is in excellent agreement with the value of 250 ± 15 cm^{-1} found here. The theoretical frequency derives further support from the observed[30] width of the CO rotational distribution. The CH_2 wagging frequency at the CH_2CO transition state ap-

pears to be 20% lower than calculated. The barrier for the hindered internal rotation of ketene at the transition state is found to be 240 cm^{-1} when a sinusoidal potential function as in Eq. (11) is assumed. This is 35% lower than the best *ab initio* value of 384 cm^{-1}.[38] Similarly, the barrier height for the reaction itself, 3.06 kcal/mol, is a kcal or so less than the best theoretical estimate.[38] Thus the actual transition state is found to be somewhat looser than predicted by the *ab initio* calculations.

The density of vibrational states of the excited reactant and the number of strongly coupled triplet levels, g_t, control the step height in the RRKM fits to measured rate constants. The Whitten–Rabinovitch approximation gives a good estimation for the ratio of the densities of CH_2CO and CD_2CO reactant states. The absolute values for the density of states for CH_2CO and CD_2CO are found to be $1.11 g_t$ and $1.19 g_t$ times higher than predicted by the Whitten–Rabinovitch approximation for energies between 28 200 and 28 700 cm^{-1}. Recent *ab initio* work on S_0 ketene gives densities of states in the range of 1–1.5 times the harmonic density.[57] This would suggest that g_t is closer to 1 than to 3. A g_t value of 3 would imply a density of states some 3.3 times larger than harmonic. Those few molecules for which experimental data exist,[13–18] exhibit even greater excesses in density of states, five to ten times harmonic. Thus there is no firm basis on which to select values for g_t and $\rho(E)$.

It is clear from comparison of the experimental data with RRKM theory that there is significantly more to be learned about the dynamics of passage through the transition state. A quantum mechanical treatment of the dynamics including coupling of the reaction coordinate to the coupled rovibrational degrees of freedom orthogonal to it will be necessary. For this treatment to be meaningfully compared with experiment, the *ab initio* potential energy surface must be mapped out through the full spread of energetically accessible bond angles near the transition state. In order to interpret experiments in which the initial rotational and nuclear spin states are fully selected, *ab initio* results are needed for the direction of the transition dipole moment vector for the UV excitation and for the magnitudes of the intersystem crossing matrix elements. Ultimately, the shapes of steps, their dependence on J and K, and the symmetries of transition-state vibrational levels along with accurate dynamical calculations will provide a clear picture of molecular dynamics in the region of the transition state.

ACKNOWLEDGMENTS

[1] H. Eyring, J. Chem. Phys. **3**, 107 (1935); E. Z. Wigner, Phys. Chem. Abstr. B **15**, 203 (1932); M. G. Evans and M. Polanyi, Trans. Faraday Soc. **31**, 875 (1935).

[2] J. Z. H. Zhang and W. H. Miller, J. Chem. Phys. **91**, 1528 (1989).

[3] D. C. Chatfield, R. S. Friedman, D. G. Truhlar, B. C. Garrett, and D. W. Schwenke, J. Am. Chem. Soc. **113**, 486 (1991).

[4] W. H. Miller, Proceedings of The Robert A. Welch Foundation 38th Conference on Chemical Research (to be published, 1995).

[5] W. H. Miller, Acc. Chem. Res. **26**, 174 (1993).

[6] T. Seideman and W. H. Miller, J. Chem. Phys. **97**, 2499 (1992).

[7] U. Manthe and W. H. Miller, J. Chem. Phys. **99**, 3411 (1993).

[8] C. Leforestier and W. H. Miller, J. Chem. Phys. **100**, 733 (1994).

[9] J. M. Bowman, Chem. Phys. Lett. **141**, 545 (1987).

[10] D. Wang and J. M. Bowman, J. Phys. Chem. **98**, 7994 (1994).

[11] S. L. Mielke, G. C. Lynch, D. G. Truhlar, and D. W. Schwenke, J. Phys. Chem. **98**, 8000 (1994).

[12] R. A. Marcus and O. K. Rice, J. Phys. Colloid Chem. **55**, 894 (1951); R. A. Marcus, J. Chem. Phys. **20**, 359 (1952).

[13] E. Abramson, R. W. Field, D. Imre, K. K. Innes, and J. L. Kinsey, J. Chem. Phys. **83**, 453 (1985); R. L. Sundberg, E. Abramson, J. L. Kinsey, and R. W. Field, *ibid*. **83**, 466 (1985).

[14] Y. S. Choi and C. B. Moore, J. Chem. Phys. **97**, 1010 (1992).

[15] W. F. Polik, D. R. Guyer, and C. B. Moore, J. Chem. Phys. **92**, 3453 (1990).

[16] A. Geers, J. Kappert, F. Temps, and W. Wiebrecht, Ber. Bunsenges. Phys. Chem. **94**, 1219 (1990).

[17] J. Miyawaki, K. Yamanouchi, and S. Tsuchiya, J. Chem. Phys. **99**, 254 (1993).

[18] S. I. Ionov, H. F. Davis, K. Mikhaylichenko, L. Valachovic, R. A. Beaudet and C. Wittig, J. Chem. Phys. **101**, 4809 (1994).

[19] C. E. Dykstra, Annu. Rev. Phys. Chem. **32**, 25 (1981); C. W. Bauschlicher, S. R. Langhoff, and P. R. Taylor, Adv. Chem. Phys. **77**, 103 (1990).

[20] F. F. Crim, Annu. Rev. Phys. Chem. **35**, 657 (1984).

[21] H. Reisler and C. Wittig, Annu. Rev. Phys. Chem. **37**, 307 (1986).

[22] W. H. Green, C. B. Moore, and W. F. Polik, Annu. Rev. Phys. Chem. **43**, 591 (1992).

[23] E. R. Lovejoy, S. K. Kim, and C. B. Moore, Science **256**, 1542 (1992).

[24] L. R. Khundkar, J. L. Knee, and A. H. Zewail, J. Chem. Phys. **87**, 77 (1987); S. J. Klippenstein, L. R. Khundkar, A. H. Zewail, and R. A. Marcus, *ibid*. **89**, 4761 (1988).

[25] G. A. Brucker, S. I. Ionov, Y. Chen, and C. Wittig, Chem. Phys. Lett. **194**, 301 (1992); S. I. Ionov, G. A. Brucker, C. Jaques, Y. Chen, and C. Wittig, J. Chem. Phys. **99**, 3420 (1993).

[26] J. Miyawaki, K. Yamanouchi, and S. Tsuchiya, Chem. Phys. Lett. **180**, 287 (1991).

[27] W. H. Green, I-C. Chen, and C. B. Moore, Ber. Bunsenges. Phys. Chem. **92**, 389 (1988); I-C. Chen, W. H. Green, and C. B. Moore, J. Chem. Phys. **89**, 314 (1988).

[28] W. H. Green, A. J. Mahoney, Q.-K. Zheng, and C. B. Moore, J. Chem. Phys. **94**, 1961 (1991).

[29] S. K. Kim, Y. S. Choi, C. D. Pibel, Q.-K. Zheng, and C. B. Moore, J. Chem. Phys. **94**, 1954 (1991).

[30] I-C. Chen and C. B. Moore, J. Phys. Chem. **94**, 269 (1990).

[31] I-C. Chen and C. B. Moore, J. Phys. Chem. **94**, 263 (1990).

[32] E. R. Lovejoy, S. K. Kim, R. A. Alvarez, and C. B. Moore, J. Chem. Phys. **95**, 4081 (1991).

[33] E. R. Lovejoy and C. B. Moore, J. Chem. Phys. **98**, 7846 (1993).

[34] I. Garcia-Moreno, E. R. Lovejoy, and C. B. Moore, J. Chem. Phys. **100**, 8890 and 8902 (1994).

[35] R. Hilbig and R. Wallenstein, IEEE J. Quant. Electron. **17**, 1566 (1981).

[36] C. D. Pibel, Ph.D. thesis, University of California at Berkeley, 1992.

[37] R. N. Dixon and G. H. Kirby, Trans. Faraday Soc. **62**, 1406 (1966); R. G. W. Norrish, H. G. Crone, and O. Saltmarsh, J. Chem. Soc., 1533 (1933).

[38] W. D. Allen and H. F. Schaefer, III, J. Chem. Phys. **89**, 329 (1988); **84**, 2212 (1986).

[39] J. W. Rabalais, J. M. McDonald, V. Scherr, and S. P. McGlynn, Chem. Rev. **71**, 73 (1971).

[40] W. F. Polik, D. R. Guyer, C. B. Moore, and W. H. Miller, J. Chem. Phys. **92**, 3471 (1990); R. Hernandez, W. H. Miller, C. B. Moore, and W. F. Polik, *ibid*. **99**, 950 (1993).

[41] C. G. Stevens and J. C. D. Brand, J. Chem. Phys. **58**, 3324 (1973); J. C. D. Brand and C. G. Stevens, *ibid*. **58**, 3331 (1973).

[42] C. C. Lin, Rev. Mod. Phys. **31**, 841 (1959).

[43] E. B. Wilson, J. Chem. Rev. **27**, 11 (1940); B. L. Crawford, J. Chem. Phys. **8**, 273 (1940).

[44] G. Brocks, A. van der Avoird, B. T. Sutcliffe, and J. Tennyson, Mol. Phys. **50**, 1025 (1983).

[45] P. A. Stockman, R. E. Bumgarner, S. Suzuki, and G. A. Blake, J. Chem. Phys. **96**, 2496 (1992).

[46] W. H. Miller, J. Am. Chem. Soc. **101**, 6810 (1979).

[47] P. D. Mallinson and L. Nemes, J. Mol. Spectrosc. **59**, 470 (1976).

[48] H. S. Johnston, *Gas Phase Reaction Rate Theory* (Ronald, New York, 1966).

[49] C. Eckart, Phys. Rev. **35**, 1303 (1930).

[50] G. Z. Whitten and B. S. Rabinovitch, J. Chem. Phys. **38**, 2466 (1963).

[51] C. B. Moore and G. C. Pimentel, J. Chem. Phys. **38**, 2816 (1963).

[52] W. H. Miller, J. Am. Chem. Soc. **105**, 216 (1983).

[53] W. Nadler and R. A. Marcus, Chem. Phys. Lett. **144**, 24 (1988).

[54] S. J. Klippenstein and R. A. Marcus, J. Chem. Phys. **91**, 2280 (1989); **93**, 2418 (1990).

[55] P. R. Bunker, P. Jensen, W. P. Kraemer, and B. Beardsworth, J. Chem. Phys. **85**, 3724 (1986); P. Jensen and P. R. Bunker, *ibid*. **89**, 1327 (1988).

[56] P. R. Bunker and P. Jensen, J. Chem. Phys. **79**, 1224 (1983).

[57] S. J. Klippenstein, A. L. L. East, and W. D. Allen, J. Chem. Phys. **101**, 9198 (1994) and A. L. L. East, W. D. Allen, and S. J. Klippenstein, *ibid*.